

Comparing gravitational waves from nonprecessing and precessing black hole binaries in the corotating frame

L. Pekowsky^{1,*}, R. O’Shaughnessy^{2,†}, J. Healy¹, and D. Shoemaker¹

¹*Center for Relativistic Astrophysics, Georgia Tech, Atlanta, GA 30332, USA and*

²*Center for Gravitation and Cosmology, University of Wisconsin-Milwaukee, Milwaukee, WI 53211, USA*

Previous analytic and numerical calculations suggest that, at each instant, the emission from a precessing black hole binary closely resembles the emission from a nonprecessing analog. In this paper we quantitatively explore the validity and limitations of that correspondence, extracting the radiation from a large collection of **191** generic black hole binary merger simulations both in the simulation frame and in a corotating frame that tracks precession. To a first approximation, the corotating-frame waveforms resemble nonprecessing analogs, based on similarity over a band-limited frequency interval defined using a fiducial detector (here, advanced LIGO) and the source’s total mass M . By restricting attention to masses $M \in 100, 1000 M_\odot$, we insure our comparisons are sensitive only to our simulated late-time inspiral, merger, and ringdown signals. In this mass region, every one of our precessing simulations can be fit by some physically similar member of the **IMRPhenomB** phenomenological waveform family to better than 95%; most fit significantly better. The best-fit parameters at low and high mass correspond to natural physical limits: the pre-merger orbit and post-merger perturbed black hole. Our results suggest that physically-motivated synthetic signals can be derived by viewing radiation from suitable nonprecessing binaries in a suitable noninertial reference frame. While a good first approximation, precessing systems have degrees of freedom (i.e., the transverse spins) which a nonprecessing simulation cannot reproduce. We quantify the extent to which these missing degrees of freedom limit the utility of synthetic precessing signals for detection and parameter estimation.

I. INTRODUCTION

Coalescing comparable-mass black hole binaries are among the most likely and useful sources of gravitational waves for existing and planned gravitational wave detectors like LIGO [1], Virgo, [2], the Einstein telescope [3], and LISA [4, 5]. For sources in a suitable mass range, the signal these detectors receive contains significant features from the late-stage, strong-field dynamics of the black hole merger. Only full numerical simulations of Einstein’s equations can provide first-principle models for this epoch, including all dynamics and emission [6, 7]. Given the large computational cost per simulation, relatively few well-determined models have been produced. Most models thoroughly explored the physics and waveform from nonprecessing binary systems [8–10]. By contrast, relatively few simulations of binaries with more generic spins have been published¹ and even fewer have provided their gravitational wave signal [14–17].

Generic precessing black-hole binaries produce a rich multimodal gravitational wave signal during their inspiral and merger. To simplify the interpretation of these signals, several authors have proposed transforming the results of numerical simulations, computed in the simulation frame, into a *corotating frame* [14, 18–21]. Empirically, a corotating frame demonstrably simplifies (and

dramatically reduces in number) the modes needed to describe the gravitational wave signal, even during and after merger. On the other hand, post-Newtonian expressions for the strain also naturally decompose into two factors: an “instantaneous” factor describing corotating emission, transformed by a rotation; see, e.g., [22, 23]. A corotating frame therefore simplifies the comparison of different simulations to one another; to post-Newtonian expressions; and to phenomenological or analytic models. Additionally, studies of how precession-induced modulations impact low-mass [24] and high-mass [14] detection strategies also naturally express their results in terms of corotating frame modes and trajectories. The nonprecessing search strategies currently being used miss precessing signals, roughly in proportion to two factors: (a) how much the signal precesses (geometrically) [25] and (b) how much the corotating-frame precessing waveform resembles some nonprecessing signal model in the search [14, 21, 24].

In this paper we compare the gravitational wave signal from the merger of a generic precessing black hole binary, expressed in a corotating frame, to nonprecessing merger waveforms. In this special frame, a precessing merging binary emits radiation that closely resembles the signal from a nonprecessing analog, for sufficiently short epochs. We determine the nonprecessing configuration that best fits the corotating-frame’s (2,2) mode, as a function of reference mass. Though tuned to one mode, selected examples suggest that the best-fit simulation usually reproduces *multiple* modes for a comparable epoch. This correspondence suggests a simple kludge to reproduce precessing merger signals, proposed directly or implicitly by authors who proposed the construction of a corotat-

*Electronic address: larne.pekowsky@physics.gatech.edu

†Electronic address: oshaughn@gravity.phys.uwm.edu

¹ Though many simulations have been performed in the analysis of merger recoil kicks, in many cases their gravitational wave signal has not been described in detail [6, 11–13].

ing frame [14, 18–21]. If an appropriate time-dependent rotation is known, then a suitable *nonprecessing* source combined with a time dependent rotation generates an approximate synthetic precessing waveform. We assess this procedure constructively, comparing the line-of-sight waveforms generated by a real precessing system and a synthetic analog. This procedure can synthesize good approximations to short waveforms from precessing black hole binaries, using physically-motivated choices for the precession rate and inspiral-merger-ringdown signal.

In the most directly comparable study, Schmidt et al. [21] applied a similar procedure to a small sample of precessing merger waveforms, derived via a post-Newtonian approximation. As expected from the functional form of the post-Newtonian inspiral signal [23], they found that the (post-Newtonian) corotating-frame signal nearly matched² emission from nonprecessing binaries with nearly-identical physical parameters. In short, this study provided concrete examples to suggest both that the inspiral signal could be efficiently represented in the corotating frame using a nonprecessing signal with nearly identical physical parameters; by implication, suitable hybrid precessing inspiral-merger-ringdown signals follow by adjoining precessing post-Newtonian and numerical relativity signals in the corotating frame. By contrast, our study assesses the similarity between our simulations’ corotating-frame signal and well-studied models for the inspiral and merger of nonprecessing binaries. Specifically, we employ many (191) generic merger signals; adopt a physically-motivated diagnostic to assess waveform similarity; demonstrate that even the merger phase of generic precessing signals resembles nonprecessing binaries, in a corotating frame; and, critically, identify and systematic limits to the accuracy of a corotating-frame approximation.

While a good zeroth approximation, this procedure does omit physics. Nonprecessing waveforms simply cannot self-consistently reproduce features tied to the system’s *kinematics*: the orbital phase versus time; the ringdown mode frequencies, set by the final black hole’s mass and spin; the ringdown mode amplitudes, which can reflect spin-orbit misalignment; et cetera. As a familiar example, in post-Newtonian calculations, time-dependent spin-orbit and spin-spin terms must be included in the orbital phase and calculated from suitable spin precession equations. In general, we find the corotating-frame waveform carries additional information (e.g., about the transverse spins) that cannot be encoded into a nonprecessing waveform. The presence of these extra degrees of freedom can explain the observationally-relevant differences between corotating-frame and simulation-frame results. Over sufficiently long time- and frequency-scales,

the differences between the corotating frame and simulation frame become startlingly apparent. In particular, early- and late-time waveforms generally resemble *different* nonprecessing systems. As a result, while corotating waveforms *approximately* resemble nonprecessing modes, they do so only for short periods in time and frequency. In practice, however, real gravitational wave data analyses are also limited to a narrow frequency interval and one line of sight. Using observationally-motivated diagnostics to characterize differences between signals, we find nonprecessing systems are a surprisingly effective analog of generic precessing sources.

We provide an executive summary and detailed outline in Section II. In Section III we review why and how we compare simulations using only their corotating-frame (2, 2) modes; explain our notation; introduce the simulations used; and describe the IMRPhenomB model [10] we use in our studies. In Section IV we present our results of fitting the precessing system. We present our synthetic signal and include a discussion of the physics we miss in such a signal in Section V. Finally, our conclusions are presented in Section VI. For interested readers, we include two appendices. Appendix A describes the previously-developed tools and notation used in this paper to compare detected gravitational waves and to extract a preferred direction from a precessing binary; and Appendix B, which describes the simulations performed and numerical tests we adopted to build quantitative confidence in our results.

II. EXECUTIVE SUMMARY AND DETAILED OUTLINE

As shown by Figure 1, the pre- and post-merger leading-order emission from each simulation is well-fit by *some* nonprecessing inspiral-merger-ringdown model, in the corotating frame. The procedure we employ to compare two signal models is described in Section III. Specifically, for each of the simulations in our sample, described at length in Appendix B and enumerated in Table I, we have transformed to a corotating frame using a suitable time-dependent rotation $R(t)$, then extracted the (angular) $(l, m) = (2, 2)$ mode time series $[R^{-1}\psi_4]_{2,2}(t) \equiv \int d\Omega R^{-1}\psi_4 Y_{2,2}^{(-2)}(\hat{n})^*$ of the Weyl scalar, as projected onto spin-weight -2 harmonics. For each possible mass $M \in 100 - 1000M_\odot$,³ we compare this time series with all possible IMRPhenomB phenomenological inspiral-merger-ringdown waveforms $\psi_{4PB}(\lambda)$ for

² Schmidt et al. [21] adopt a completely different definition of “match”, based on a single polarization and a white power spectrum. Their quantitative statements cannot be directly compared with our own.

³ As noted in the introduction and quantified in the Appendix, the duration of our numerical simulations was used to select a mass interval, such that only our numerical simulations would significantly influence the comparisons we performed. Physically, at these masses only the late stages of inspiral and merger would be accessible to the advanced LIGO detector, at plausible signal amplitudes.

nonprecessing binaries [10]. The mass range is chosen at the low end to avoid the use of hybrid waveforms in this study, and at the high end to ensure the inclusion of ringdown. Motivated by data analysis, we compare signals with a complex “overlap”, maximized over time and polarization [26, 27]; see Appendix A for a brief review. We adopt a fiducial advanced LIGO noise curve (zero detuned high power; see [28]) and perform integrals over 5 – 2000 Hz.⁴ Using differential evolution [29], a hill-climbing algorithm, we select the best-fitting nonprecessing (IMRPhenomB) mass, spin, and mass ratio for each precessing binary merger simulation and mass. The best-fit parameters are denoted by λ_{PB} and the best-fit match is denoted $P_{\text{max,corot}}$:

$$P_{\text{max,corot}} \equiv \max_t \frac{|\langle [R^{-1}\psi_{4NR}]_{2,2} | [\psi_{4PB}(t, \lambda_{PB})]_{2,2} \rangle|}{|R^{-1}\psi_{4NR}| |\psi_{4PB}(\lambda_{PB})|}. \quad (1)$$

Figure 1 shows the fraction of simulations with match $P_{\text{max,corot}}$ [Eqs. (A7, A8)] greater than a specified threshold. Most have a match within a few percent of unity; and, therefore, a precessing model and its nonprecessing analog would appear very similar to a gravitational wave detector network with plausible signal amplitude [27].

As described in Section IV, the best-fitting nonprecessing parameters depend on precisely which time and frequency interval we adopt for comparison. For the data-analysis-driven diagnostic used here, the best-fitting parameters depend on the *mass* adopted for the precessing binary. Roughly speaking, at low mass the best-fitting nonprecessing model has similar mass ratio and “effective spin” [10, 30–32]. When fitting the IMRPhenomB model to our data, our results suggest the best-fitting binary has the same value of the IMRPhenomB “effective spin” parameter χ_{PB} ; see Section IV. For illustration, Figure 2 shows how χ_{PB} depends on simulation mass, for a one-parameter family of equal mass binary mergers.

Conversely, at high mass the signal produced by the simulation and any nonprecessing model is dominated by quadrupole radiation from the final black hole. Inevitably, the best-fitting nonprecessing models must predict comparable final states.

Despite adopting a phenomenologically-motivated comparison, our method identifies nontrivial, physically significant relationships between precessing and nonprecessing signals. As demonstrated in Section IV, the best-fit nonprecessing model to the early time (here, low mass) signal has the physically-anticipated parameters needed to reproduce a common orbital phase evolution: similar mass ratio and “effective spin”. For this reason,

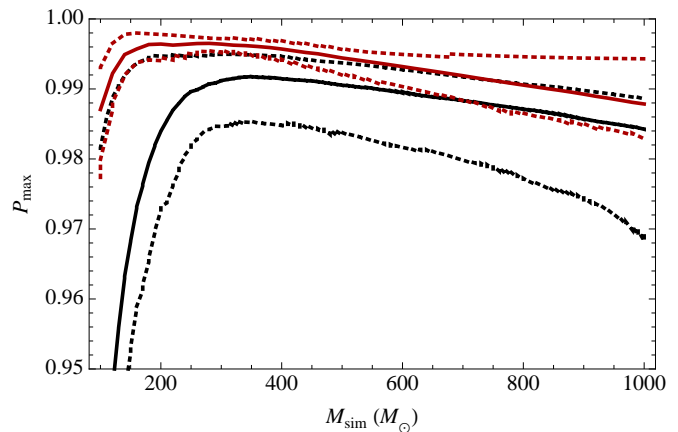


FIG. 1: **Precessing binaries resemble nonprecessing binaries:** Distribution of best fit complex overlap $P_{\text{max,corot}}$ [Eq. (1)] between the IMRPhenomB and our simulated signals of mass M . The solid black curve shows the median-probability overlap P_{max} at each mass: half of our precessing simulations have a fitting factor above the black solid line at each mass; the dotted black curves show the 90% confidence interval, estimated from our set of **191** simulations. For comparison, the red solid and dotted curves show the median fitting factor and 90% confidence interval estimated from **58** nonprecessing simulations; these simulations are not included in the previous list. All calculations are performed by comparing the two models’ (2, 2) modes, each in a suitable corotating frame. Our simulations have significantly different initial conditions and hence durations: many shorter simulations do not have enough data to reliably estimate the waveform and hence P for $M \lesssim 250M_\odot$. Our longer simulations, including the nonprecessing simulations, are relatively well-fit by the IMRPhenomB model down to $\simeq 100M_\odot$.

we anticipate the corotating-frame modes can be naturally extended to arbitrarily early times via “hybridization” with conventional post-Newtonian or effective-one-body models for the early inspiral. Even though we only fit the (2, 2) mode, detailed followup of a handful of similar systems suggests the best-fitting parameters reproduce several modes simultaneously. Indeed, the striking similarity illustrated by the top panel of Figure 4 and first noted in Figure 12 of Schmidt et al. [18] was used to motivate detailed analysis of the corotating frame. Unfortunately, we only possess continuously-parameterized models for one mode from a generic nonprecessing binary; we defer a detailed quantitative analysis of multiple modes to a future study.

As noted in Section V, this formal similarity in a non-inertial frame is directly relevant to physical observers in the inertial frame, each limited to a single fixed line of sight that does not corotate with the binary. A nonprecessing signal, combined with a suitable rotation, will generate a reasonable facsimile of a precessing signal, in the *observer’s frame*. As a result, even though detailed simulations of precessing binaries are computationally expensive, a computationally trivial procedure can generate plausible precessing inspiral-merger-

⁴ For binary masses $M < 300M_\odot$ ($40 \text{ Hz}/f_{\text{low}}$), our results are not strongly sensitive to the lower frequency limit adopted for the integrand. We adopt $f_{\text{low}} = 5 \text{ Hz}$, to insure only the detector noise power spectrum, and not arbitrary choices for f_{low} , determines our results at high mass.

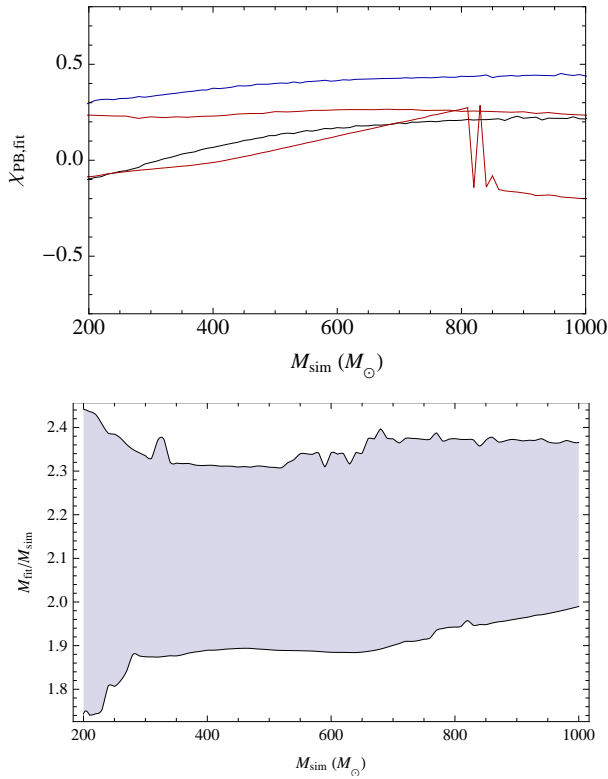


FIG. 2: **Best-fit nonprecessing parameters depend on precessing parameters and mass, and can differ from the simulation parameters:** *Top panel:* For selected simulations studied in this work, a plot of the best-fitting effective spin χ_{PB} versus the simulated binary’s mass. The best-fit effective spin changes as a function of mass: while the initial and final state separately resemble a nonprecessing system, no single nonprecessing system fits the whole time-dependent corotating-frame mode. Instead, the best-fitting parameters interpolate (sometimes discontinuously) between the initial and final state. Colors indicate the Sq series (black); the Tq series (blue); and the short simulations of the T series (red). *Bottom panel:* For all simulations used in this work, the ratio $M_{\text{fit}}/M_{\text{sim}}$ between the fitted and simulated mass. As indicated by the shaded region, the best-fitting mass can differ by up to $\simeq 10\%$ from the simulated mass.

ringdown signals. To demonstrate this agreement, Figure 3 uses the *best-fit* corotating-frame IMRPhenomB parameters λ_{PB} derived in the corotating frame; generates a time-domain corotating-frame signal consisting of only the IMRPhenomB $(2, \pm 2)$; transforms to the corotating frame to create a synthetic multimodal signal $R(t)\psi_{4PB}(t, \hat{n})$; and calculates the complex match P_{max} between the simulation-frame $(2, 2)$ modes of the synthetic signal and the original precessing NR simulation

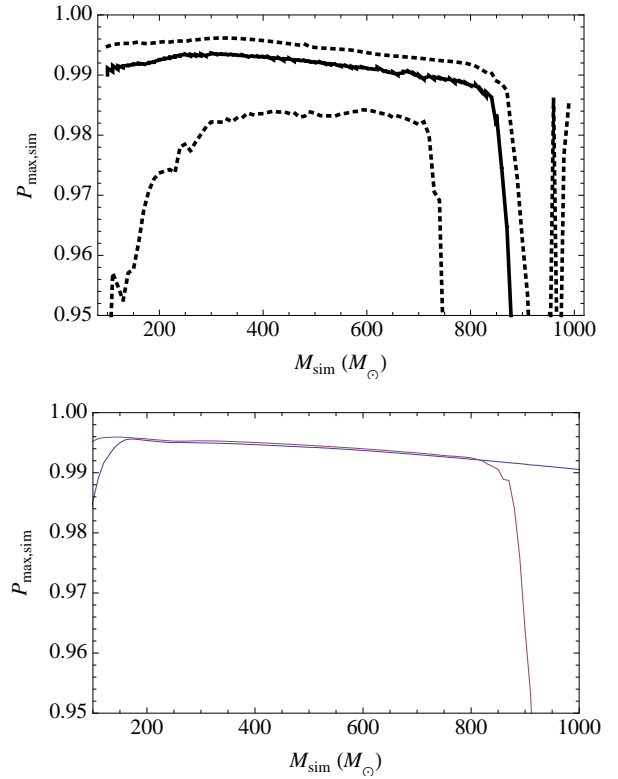


FIG. 3: **Synthetic precessing waveforms resemble precessing waveforms:** *Top panel:* The distribution of $P_{\text{max},\text{sim}}$ [Eq. (2)], the match between $\psi_{4NR,2,2}$ and $R\psi_{4PB}$, a synthetic precessing signal derived by applying a known time-dependent rotation to a best-fitting IMRPhenomB waveform. This distribution is effectively identical to that shown in Figure 1. *Bottom panel:* For the Sq(1.5, 0.6, 45) simulation, a plot of the match $P_{\text{max},\text{sim}}$ and $P_{\text{max},\text{corot}}$ [Eq. (1)]. As this example illustrates, except for very high masses $P_{\text{max},\text{corot}} \simeq P_{\text{max},\text{sim}}$. To avoid over-weighting the single worst case, which has $P_{\text{max},\text{corot}} \simeq 0.95$ for all masses, we have explicitly eliminated all five resolutions of the strongly-precessing Sq(4,0.6,270,9) and the equivalent Tq(4,0.6,90,9) from this comparison. By contrast, all resolutions and iterations are included in Figure 1.

to which the corotating-frame mode was fit⁵:

$$P_{\text{max},\text{sim}} = \max_t \frac{|\langle \psi_{4NR,2,2} | [R\psi_{4PB}(t, \lambda_{PB})]_{2,2} \rangle|}{|\psi_{4NR,2,2}| | [R\psi_{4PB}(\lambda_{PB})]_{2,2}|} \quad (2)$$

At low mass $M \lesssim 1700M_{\odot}$, these two quantities agree: $P_{\text{max},\text{corot}} \simeq P_{\text{max},\text{sim}}$. As expected, at high mass these two quantities increasingly disagree. This disagreement does not reflect intrinsic dissimilarity between non-

⁵ In our investigations, we constructed a family of synthetic precessing signals, unique up to overall mass scale M . The figures provided in the text describe the performance of the best-fitting member of that one-parameter family. We obtain almost identical results if the procedure described in the text is followed verbatim.

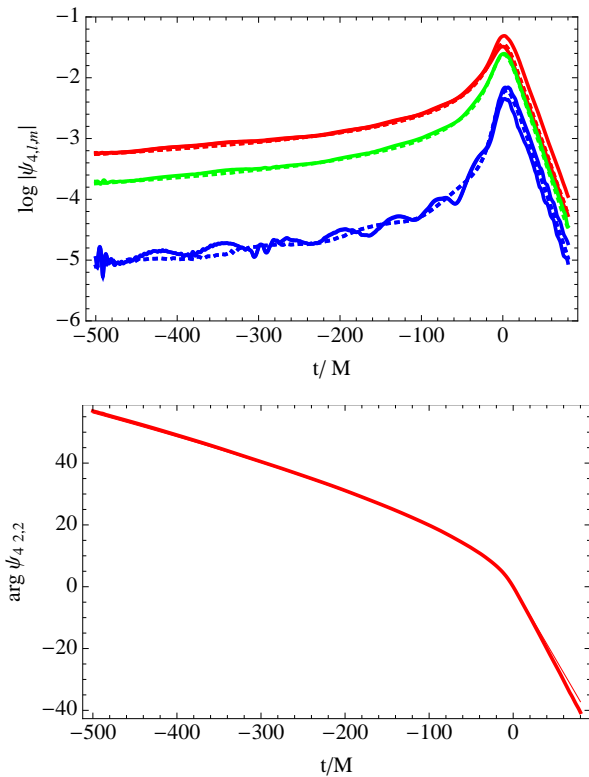


FIG. 4: **Corotating signal resembles nonprecessing signal** : Comparison of $|rR^{-1}\psi_{4,l,m}|$ (top panel) and $\arg R^{-1}\psi_{4,2,2}$ (bottom panel) for a *nonspinning* $q = 4$ simulation (dotted) with the corotating waveform from the Sq(4,0.6,270,9) simulation (thick). The colored curves correspond to the $(2, \pm 2)$ modes (red, solid); the $(2, \pm 1)$ modes (blue); and the $(3, 3)$ mode (green). A timeshift has been applied to align the two simulations. This comparison shows several modes from the same nonprecessing simulation reproduce the corotating frame modes from another [18].

precessing and precessing signals. Instead, it reflects our strict application of the best-fit parameters derived from the corotating frame to a slightly different problem: reproducing ψ_{4NR} in the simulation frame. At high mass, slightly different choices for ψ_{4PB} are needed to optimally reproduce the NR signal in each frame.⁶ In special cases like Figure 4, a single nonprecessing model can approximate the entire signal.

Our calculations demonstrate these inexpensive models provide a fast, surprisingly accurate model for generic precessing signals. Moreover, though not described in detail here, the rotation operation $R(t)$ can be easily mod-

⁶ Though the Fourier transform of $R(t)\psi_4(t)$ is well-approximated by $R(t(f))\psi_4(f)$ at early times, when the rotation operation changes slowly, at late times a stationary-phase approximation is not sufficiently accurate for our purposes. Equivalently, the rotation needed at late times oscillates on a timescale comparable to the quasinormal mode frequency spacing.

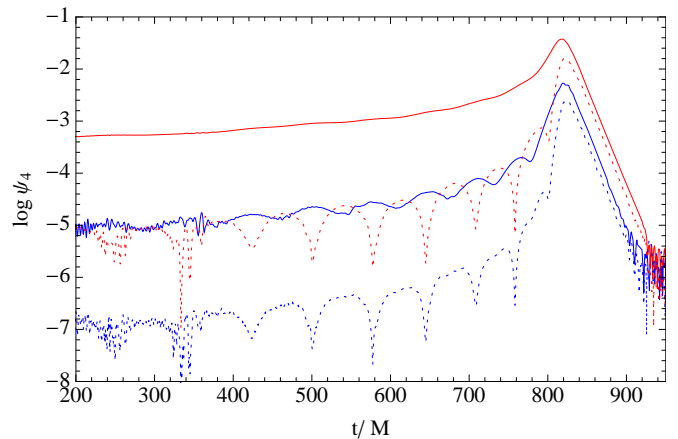


FIG. 5: **Precessing systems break reflection symmetry in the corotating frame**: For the Sq(4,0.6,90,9) simulation provided in [14], a plot of the reflection-symmetric (solid) and reflection-antisymmetric (dotted) parts of the corotating-frame $l = 2$ modes, for $m = \pm 2$ (red) and ± 1 (blue); see Eq. (3). This figure suggests that precessing binaries radiate in a way unlike any nonprecessing binary, even one viewed in a noninertial frame; that this missing physics has a comparable effect to higher harmonics like the $(2, \pm 1)$ modes (e.g., dotted red vs solid blue); and that both reflection symmetry breaking and higher harmonics are required to accurately model the merger phase of generic precessing binaries.

eled and fit, particularly in a frame aligned with the total angular momentum. In principle, comparisons like our own allow fits to functions $\lambda_{PB}(\lambda)$ and $R(t|\lambda)$, hence producing a “synthetic waveform” $R(\lambda)\psi_{4PB}(\lambda_{PB})$. Our analysis suggests these “synthetic waveforms” can be used as a simple method with which to prototype data analysis strategies for precessing, multimodal sources. However, because nonprecessing models omit critical physics, particularly in the high-mass regime emphasized in this paper, we do not recommend high-precision calibration of these synthetic waveforms, particularly if that calibration is limited to a study of only the leading-order $(2, 2)$ mode.

Even when viewed in a rotating frame, a nonprecessing binary retains its intrinsic symmetries: spins aligned with the orbital plane. Without precessing spins to break symmetry and source other multipoles, the emitted radiation has strong symmetries: reflection symmetry through the orbital plane, insuring that at every instant the binary radiates equal and opposite left- and right-handed radiation, in mirror-symmetric directions. By contrast, our previous calculations [14] and long experience with black hole superkicks demonstrate that precessing black holes radiate *asymmetrically*, emitting preferentially right-handed or left-handed radiation at any instant. Equivalently, even in the corotating frame, precessing binaries break reflection symmetry through the orbital plane. In Section V we use reflection symmetry to quantify the extent to which a nonprecessing model omits critical physics. To quantify the magnitude to

which reflection symmetry is broken, we use conjugation symmetry to define CP-odd ($b_{l,m}(t) = -(-1)^l b_{l,-m}(t)^*$) and CP-even ($a_{l,m}(t) = (-1)^l a_{l,-m}(t)^*$) parts of the corotating-frame Weyl scalar ($R^{-1}\psi_4$):

$$[R^{-1}\psi_4]_{l,m} = a_{l,m} + b_{l,m} \quad (3)$$

Globally, this specific symmetry \mathcal{C} corresponds to a reflection symmetry through the $z = 0$ plane:

$$\mathcal{C}\psi_4 \equiv \psi_4(\pi - \theta, \phi)^* \quad (4)$$

$$\begin{aligned} &= \sum_{l,m} [a_{l,-m} - b_{l,-m}] [(-1)^l Y_{l,m}^{(-2)}(\pi - \theta, \phi)]^* \\ &= \sum_{l,m} [a_{l,-m} - b_{l,-m}] Y_{l,-m}^{(-2)}(\theta, \phi) \end{aligned} \quad (5)$$

For a nonprecessing binary, the CP-odd term $b_{l,m} = 0$. Using a concrete precessing example, Figure 5 shows the CP-even (solid) and CP-odd (dotted) parts of the leading-order corotating-frame angular modes $\psi_{4l,m}$. Comparing the red dotted and solid lines, this figure demonstrates that after merger, the CP-odd part of the dominant mode is significant. In other words, this figure shows that, to accurately describe this binary's emission versus time and angle, we *must* include a CP-odd part – a part no nonprecessing signal could ever produce! More broadly, because a precessing binary has more physics, its signal remains more complicated than one from a nonprecessing binary, even in the corotating frame.

Figure 6 illustrates the practical implications of these asymmetries. This figure shows the match $P_{\text{max,corot}}$ for a one-parameter family of high-symmetry simulations: binaries with $m_1 = m_2$, $\vec{a}_1 = a\hat{n}(\theta, \phi)$, and $\vec{a}_2 = a\hat{n}(\theta, \phi + \pi)$ as a function of ϕ . By construction, each member of this one-parameter family has an identical projection of the spin along the orbital angular momentum axis (χ_{PB}) and more generally identical total spin $\mathbf{S}_1 + \mathbf{S}_2$; evolves without precession of the orbital plane; and produce black holes whose final mass and spin does not change significantly with ϕ [Table I]. Moreover, these binaries produce similar *symmetric* radiation $a_{2,2}$ for all orientations ϕ . To quantify this similarity, Figure 6 shows the value of

$$P_{\text{max,NR,a}} = \max_t \frac{|\langle a_{2,2} | a'_{2,2}(t) \rangle|}{|a_{2,2}| |a'_{2,2}|} \quad (6)$$

evaluated between one reference simulation and all others, at one reference mass; the high and nearly constant match demonstrates $a_{2,2}$ is effectively independent of ϕ .⁷ Nonetheless, the total gravitational wave signal $[R^{-1}\psi_4]_{2,2} = a_{2,2} + b_{2,2}$ emitted by these binaries measurably changes with ϕ . These differences can be easily

⁷ Similar results occur at all masses. In the interests of brevity, we do not plot all of the functions $a_{2,2}(\phi)$, even though their manifest similarity is immediately apparent to the eye.

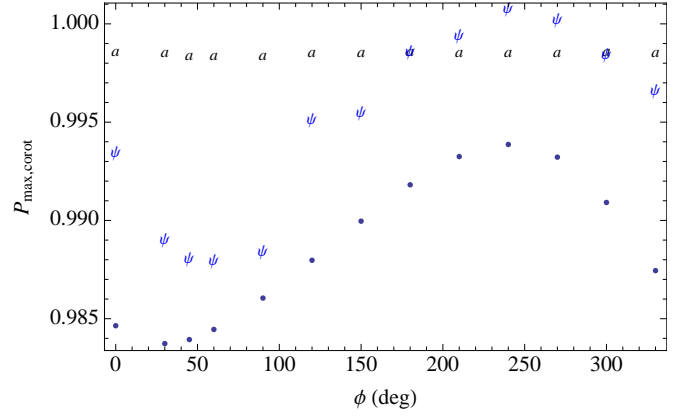


FIG. 6: Does it matter if we omit the transverse spin?: This figure demonstrates that transverse spins have a significant effect on the gravitational wave signal, via reflection-symmetry-breaking between the $(2, \pm 2)$ modes. For the special-purpose $V(a, \theta, \phi)$ family of precessing simulations described in the text and Appendix B, points show the match $P_{\text{max,corot}}$ versus the angle ϕ , for the fixed angle $\theta = 34^\circ$. For comparison, this figure uses ψ to indicate the match $P_{\text{max,NR}}$ [Eq. (7)] evaluated between the corotating-frame $(2, 2)$ mode for one member of that family [$V(0.6, 34, 240)$] and all others, directly demonstrating how much these signals differ from one another. For another comparison, this figure uses a to indicate the match $P_{\text{max,NR,a}}$ [Eq. (6)] between the reflection-symmetric part of the corotating-frame $(2, 2)$ ($a_{2,2}$) of that same simulation and all other angles ϕ . The strong variability in the first set (ψ) and lack of variability in the second (a) suggests that reflection asymmetry is the dominant source of variation between different simulations. This figure illustrates strong, generic correlations between the precise magnitude and direction of the transverse spins; reflection asymmetry between the (2 ± 2) modes in the corotating frame; and the degree of similarity between the $(2, 2)$ corotating-frame mode and conventional non-spinning approximations.

assessed simply by noting the best-fitting parameters and $P_{\text{max,corot}}$ recovered when comparing with **IMRPhenomB** vary with mass; as an example of the latter diagnostic, see the points in Figure 6. More directly, these differences can be demonstrated by computing the overlap between different simulations $[R^{-1}\psi_4]_{2,2}$ for the values ϕ, ϕ' , via

$$P_{\text{maxNR}} = \max_t \frac{|\langle [R^{-1}\psi_4]_{2,2} | [R^{-1}\psi_4']_{2,2} \rangle|}{|[R^{-1}\psi_4]_{2,2}| |[R^{-1}\psi_4']_{2,2}|} \quad (7)$$

One such example is provided by the markers labeled ψ in that figure. Figure 6 suggests the asymmetry ($b_{2,2}$) is principally responsible both for a significant fraction of the mismatch $1 - P_{\text{max,corot}}$ and for all the fluctuation in the match versus ϕ . This correlation is generic: all other generic binaries preferentially radiate asymmetrically as the spins precess, above and below the instantaneous orbital plane. To a first approximation, the dominant, symmetric part $a_{2,2}$ resembles a nonprecessing signal; a comparison between $a_{2,2}$ and **IMRPhenomB** approximately determines the best-fitting parameters. Partic-

ularly during at late times when asymmetries between $(2, \pm 2)$ become particularly significant, however, the influence of asymmetry can significantly diminish (or enhance) the similarity between nonprecessing and precessing signals – in our context, change the best-fitting IMRPhenomB parameters and match $P_{\text{max,corot}}$. Broadly speaking, our results suggest larger degrees of asymmetry between $(2, \pm 2)$ correlate with a generally larger but spin-orientation-dependent mismatch between the corotating-frame $(2, 2)$ modes and IMRPhenomB.

To summarize, our study suggests that nonprecessing signals, suitably rotated, *resemble* but cannot reproduce with high precision the gravitational wave signal from generic precessing binaries. With few exceptions,⁸ synthetic precessing signals generated from nonprecessing binaries will not be adequate for high-precision parameter estimation, unless augmented by new physics (i.e., transverse spins) and multiple harmonics. That said, given the robust similarity of nonprecessing and precessing merger signals over observationally relevant intervals, we anticipate synthetic precessing signals will be extremely useful *as plausible signals*. We strongly recommend that existing gravitational wave search strategies for high-mass merger signals test how reliably they can recover the complex multimodal from precessing binaries with $M > 100M_\odot$ using “synthetic” multimodal inspiral-merger-ringdown signals, generated simply by viewing a nonprecessing binary in a precessing frame.

Finally, motivated by previous studies and our own results [e.g., Figure 5], we anticipate that detailed parameter estimation of high-mass ($M > 100M_\odot$) binary mergers will require detailed modeling of multiple modes of generically-precessing binaries. A corotating frame and a nearly- nonprecessing CP-even approximation can reduce the number of functions to fit; in this mass region, however, higher harmonics cannot be neglected.

III. COMPARING THE COROTATING AND SIMULATION FRAME

A. Why compare nonprecessing and precessing binaries in the corotating frame?

As we will discuss at greater length in Section V, with more degrees of freedom in their underlying kinematics, precessing binary mergers never look exactly like a nonprecessing merger, even in the corotating frame. In the corotating frame, the gravitational waves from precessing binaries break symmetries and carry more information than the signal from the best-fitting nonprecessing

⁸ For special quantities constrained by symmetry, like the opening angle of the precession cone, parameter estimation should be reliable, independent of whether the corotating-frame model works well, due both to separation of timescales and due to the way polarization modulations enter into the signal

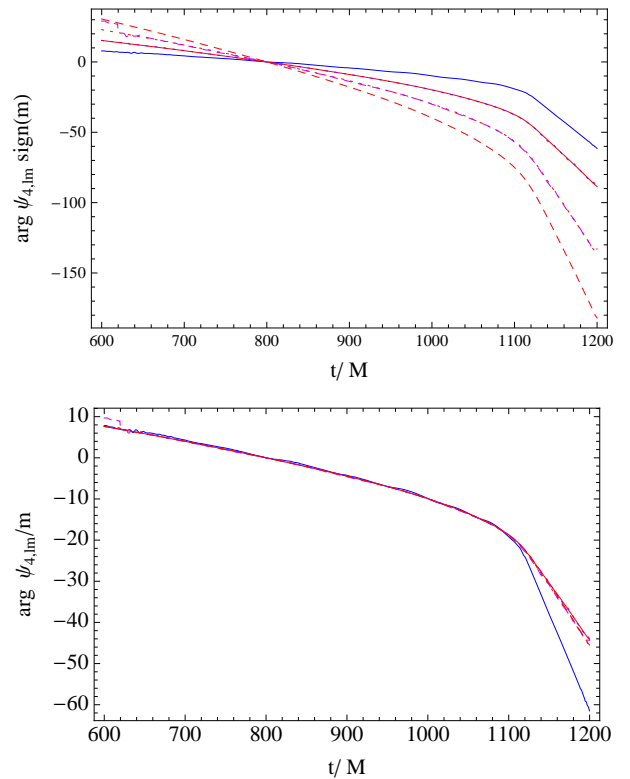


FIG. 7: Corotating modes evolve nearly in phase prior to merger: Phases of corotating modes in an absolute scale (top panel) and scaled in proportion to their angular order $\phi_{l,m}/|m|$ (bottom panel), for the Tq(2,0.6,90) simulation. To a good approximation all evolve in phase prior to merger. After merger, all angular harmonics shown continue to evolve nearly in phase, except the $(2, 1)$ mode. Colors indicate the (l, l) modes (red, with solid as $l = 2$, dotted as $l = 3$, and dashed as $l = 4$); the $(2, 1)$ mode (blue); the $(4, 3)$ mode (dashed purple); and the $(3, 2)$ mode (dotted purple).

analog. Nonetheless, the additional degrees of freedom are very difficult to excite in a quasicircular inspiral. In surprisingly many scenarios, a precessing binary may be well-approximated by the emission from a nonprecessing binary, plus a slowly-changing orientation. Qualitatively speaking, the corotating-frame mode amplitudes $R^{-1}\psi_{4l,m}$ extracted from a precessing binary have similar characteristics as the corresponding modes seen in a nonprecessing binary. In the time domain, all of the corotating-frame modes $R^{-1}\psi_4$ have smooth phase evolution and (roughly) smooth amplitude evolution.⁹ This

⁹ The corotating-frame $|R^{-1}\psi_{4l,m}|$ are weakly modulated during the inspiral, in two ways. First, the $(l, \pm m)$ modes can increase or decrease at the same time (in phase), due to either to residual eccentricity or suitable spin precession (for suitable modes). The $(l, \pm m)$ modes can increase or decrease out of phase, as precessing spins source symmetry-breaking multipole moments. For example, during inspiral the leading-order asymmetry occurs from current quadrupole radiation, sourced by the transverse spins

smooth and simple behavior in the amplitude and phase has already been noted previously [18–21]. As a first approximation, we also find corotating modes resemble suitable nonprecessing ones; see Figure 4 as an example. Because of this correspondence, the corotating frame waveforms roughly satisfy the same symmetries as nonprecessing binaries. For example, during the inspiral the modes evolve in phase (i.e., $\propto m^{-1} \arg R^{-1} \psi_{4l,m}$); see Figure 7. More generally, all modes are approximately phase conjugate (i.e., $\arg R^{-1} \psi_{4l,m} \simeq -\arg(-1)^l R^{-1} \psi_{4l,-m}$). By contrast, as has repeatedly been demonstrated in the literature, the simulation-frame modes are both significantly different and more complicated [14, 18–21]. Except for nearly-nonprecessing binaries, the substantial differences between the corotating-frame and simulation-frame waveforms are much more significant than the relatively small numerical uncertainties in this mass regime.

In short, the corotating frame provides a significantly different, simpler waveform with many approximate symmetries. Previous experience suggests these symmetries facilitate interpretation and quantitative calculations for precessing merging binaries [14, 24]. Moreover, even though observers cannot co-rotate with the binary, analytic calculations suggest the corotating frame signal has direct observational relevance, based on separation of timescales. For example, as we highlighted in our executive summary, comparisons between the (unobservable) corotating-frame signals are directly comparable to comparisons between (observable) simulation-frame quantities: $P_{\text{max,corot}} \simeq P_{\text{max,sim}}$ [Eqs. (1,2); see Figure 3].

B. Comparing a corotating mode with a phenomenological model using a complex overlap

Following previous studies [14, 26, 27], we use a complex overlap to assess the observationally-relevant differences between two signals a, b

$$\langle a|b \rangle \equiv 2 \int_{-\infty}^{\infty} \frac{a^*(f)b(f)}{S_h(2\pi f)^4} df \quad (8)$$

where each of a, b represent some value for the outgoing Weyl scalar $\psi_{42,2} \equiv \langle 2, 2 | \psi_4 \rangle = \int [Y_{l,m}^{(-2)}]^* \psi_4 d\Omega$. see, e.g., Eq. (24) in [14] and the detailed review in Appendix A. In this work, we apply this diagnostic to pairs of signals in the corotating frame [Eq. (1)] and in the simulation frame [Eq. (2)].

C. The IMRPhenomB family as a continuous reference model

Though numerous, our numerical simulations of nonprecessing and precessing binaries only discretely sample the model space. For this reason, rather than directly compare pairs of simulations, we compare our simulations against IMRPhenomB [10], a model for $h_{2,2}$ as a function of total binary mass M , mass ratio $\eta = m_1 m_2 / (m_1 + m_2)^2$, and a single effective spin parameter χ_{PB} :

$$\chi_{\pm} \equiv \hat{L} \cdot (\mathbf{S}_1/m_1^2 + \mathbf{S}_2/m_2^2)/2 \quad (9a)$$

$$\begin{aligned} \chi_{PB} &= \hat{L} \cdot (m_1 \mathbf{S}_1/m_1^2 + m_2 \mathbf{S}_2/m_2^2)/M \\ &= [(1+\delta)(\mathbf{S}_1/m_1^2) + (1-\delta)\mathbf{S}_2/m_2^2]/2 \\ &= \chi_+ + \delta\chi_- \end{aligned} \quad (9b)$$

where $\delta = (m_1 - m_2)/M$. This model employs a physically-motivated piecewise-continuous expression for $h_{22}(f)$, expressed as an amplitude $|h_{22}|$ and phase $\arg h_{22}$. At low frequencies their expressions reproduce conventional stationary-phase approximations derived from post-Newtonian theory; conversely, at high frequencies, their amplitude model $|h_{22}(f)|$ has the Lorentzian form expected from a quasinormal mode ringdown. Parameters of this hybrid, phenomenological model were set by comparing to numerical simulations and to an extreme-mass-ratio limit. This model has been calibrated against numerical simulations; includes the effect of aligned spins; and has been made publicly-available via the `lalsimulation` toolkit. As this code provides a model for the strain (h_{PB}) rather than the Weyl scalar, we explicitly convert between representations using the Fourier transform

$$\tilde{\psi}_{4PB}(f|M, \eta, \chi_{PB}, t_{mgr}) = -\frac{1}{(2\pi f)^2} \tilde{h}_{PB}(f) \quad (10)$$

Because the inspiral and final black hole depend on the component masses and spins in distinctly different ways, no one IMRPhenomB model can reproduce a generic corotating-frame (2,2) mode for all time. For this reason, we distinguish between the simulated binary’s parameters ($M_{\text{sim}}, \eta_{\text{sim}}, \chi_{PB,\text{sim}}$) and the parameters of some best-fitting IMRPhenomB model ($M_{\text{fit}}, \eta_{\text{fit}}, \chi_{PB,\text{fit}}$).

By comparing a model against our simulations rather than comparable simulations against one another, we introduce systematic error. To quantify the degree of similarity between the IMRPhenomB model and our nonprecessing simulations, we have evaluated $P_{\text{max,sim}} = P_{\text{max,corot}}$ between this model and an array of 34 nonprecessing simulations. As indicated by the red curves in Figure 1, for most simulations and a wide range of masses, some member of the IMRPhenomB model matches each of our simulations to better than $\simeq 1 - 2\%$. The best-fitting parameters are always close to our simulation parameters.

Since IMRPhenomB was first published, other models have been developed that may even more accurately reproduce the merger of precessing binaries over a wide

being transported around the orbit. The theory underlying the latter scenario is briefly reviewed in the text and Appendix A.

range of masses and spins [8, 33]. While we have compared these models against some of our numerical simulations, in this work we limit our comparisons to the sufficiently accurate and easy-to-evaluate IMRPhenomB model.

D. In the corotating frame, nonprecessing and precessing binaries resemble one another

Figure 1 summarizes the results of our comparison between IMRPhenomB and each numerical simulation, in the corotating frame. In short, the two nearly agree: for every simulation, some nonprecessing IMRPhenomB model exists which nearly reproduces that simulation’s corotating (2, 2) mode ($[R^{-1}\psi_4]_{2,2}$) over an observationally relevant interval.

A closer investigation of Figure 1, however, suggests that systematic differences exist between corotating-frame waveforms and nonprecessing signals. In that figure, the red curves show that truly nonprecessing simulations are better fit by IMRPhenomB (red curves) than the corotating-frame signal from a precessing binary (black curves), with matches of order 1 – 3% better. This level of disagreement is large enough to be observationally accessible: typically, parameter estimation strategies can resolve differences between models when their matches differ by $1/\rho^2$, expected to be of order $\gtrsim 1/10^2$ for the first detections at signal amplitude $\rho \simeq 10$.

As highlighted in the executive summary and as we will describe in detail later, these differences between the corotating-frame and simulation-frame signal are expected on physical grounds: the real binary has more degrees of freedom, reflected in the orbit and critically current quadrupole radiation. These differences fundamentally limit the accuracy of synthetic signals that hope to reproduce precessing signals using suitably-rotated nonprecessing binaries. Equivalently, the difference between the red and black curves in Figure 1 suggests an accuracy threshold for proposals that hope to carefully calibrate such models against numerical merger signals.

For comparison, we have repeated the fitting process in the simulation frame, computing P_{\max} by directly comparing $\psi_{4PB,2,2}$ to $\psi_{4NR,2,2}$. Most of our simulations have approximately aligned initial orbital (\hat{L}) and total (\hat{J}) angular momentum directions. As a result, the fitting procedure generally finds a similar best fit P_{\max} at a similar parameter location. The small offset between the best-fit simulation frame and corotating frame parameters can be qualitatively understood: rapid in-band precession shifts the best-fit parameters by an amount proportional to the post-merger precession frequency. The question of directly comparing precessing simulations to nonprecessing models has considerable practical interest, particularly for efforts to estimate binary parameters using simple models for the merger signal. That said, the results of this comparison are beyond the scope of our current study and not provided here.

IV. UNDERSTANDING THE BEST-FIT PARAMETERS

As described above, for each simulation and mass, we have found the nonprecessing model parameters ($M_{\text{sim}}, \eta_{\text{sim}}, \chi_{PB,\text{sim}}$) such that the corotating-frame (2, 2) mode and the IMRPhenomB mode are most similar. As illustrated by Figure 2, the best-fit nonprecessing parameters are neither constant nor trivially related to the precessing binary being simulated. In fact, on physical grounds we expect and our calculations show that the best-fit nonprecessing model to evolve from a *low-mass* limit that reproduces qualitative features of the corotating-frame inspiral to a *high-mass* limit that reproduces qualitative features of the corotating-frame final black hole’s ringdown.

A. Low-mass limit

In the advanced LIGO sensitive band, the gravitational wave signal from a low mass binary $M < 300M_\odot$ is produced principally *prior* to merger, when the two objects can be distinguished as separate objects. At low mass the best-fitting nonprecessing model should resemble the initial binary, reproducing its orbital evolution. In other words, not only will the IMRPhenomB model fit, but the best-fitting model parameters are actually physical properties of the binary. Specifically, the best-fitting nonprecessing model $\psi_{4PB}(\lambda_{PB})$ should have similar mass ratio and “effective spin” [10, 30–32].

Figure 8 compares the simulation’s mass ratio η_{sim} to the best-fitting IMRPhenomB mass ratio η_{fit} for all of our long-duration simulations (i.e., an initial separation $d > 7$). To emphasize the inspiral, this figure adopts the best-fit parameters at $M = 100M_\odot$. Despite systematic differences between the IMRPhenomB model and our nonprecessing simulations (green points), this figure and Figure 1 together suggest that both nonprecessing and precessing simulations and the IMRPhenomB model all produce nearly-indistinguishable estimates for the inspiral phase of $R^{-1}\psi_{42,2}$ at the same physical parameters.

In practice, the short duration of most of our precessing simulations limits our ability to recover the inspiral signal in isolation. Equivalently, as illustrated in Figure 1, the best fit between IMRPhenomB and our precessing signals is relatively poor below $250M_\odot$. That said, because IMRPhenomB includes both inspiral and merger, we anticipate the best-fit parameters at $M = 300M_\odot$ will still correspond to binary parameters that approximate the simulated system just prior to merger, in a corotating frame; see the Appendix for further discussion. Figure 9 shows an example of the best-fitting IMRPhenomB spin parameter $\chi_{PB,\text{fit}}$ for a one-parameter family of simulations, evaluated at $M = 300M_\odot$. Given the fundamental physical differences between the IMRPhenomB model and simulations and given the mass used for comparison, we are not surprised that the best fit parameters do not lie

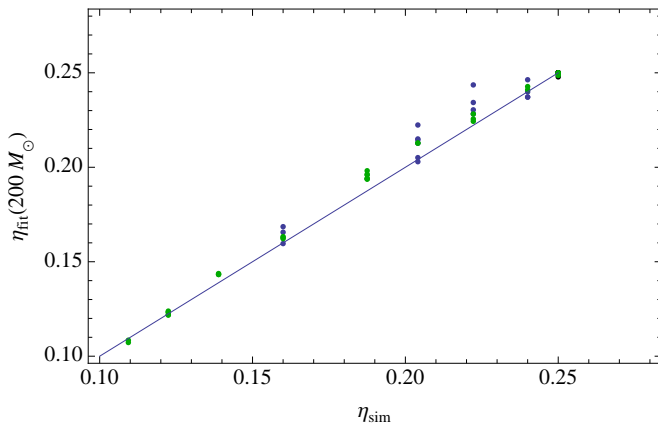


FIG. 8: **Low mass limit: Recovering the mass ratio:** At low masses and therefore early times, the best-fit corotating-frame model reflects the initial binary. These panels show comparisons between the best-fit IMRPhenomB parameter η_{fit} and the physical binary mass ratio η , using best-fit values at $M = 100M_\odot$; compare to Figure 9. This figure explicitly excludes all of our shorter simulations ($d < 7M$). Green points are nonprecessing spin-aligned systems; black points are long-duration simulations from the Sq series; and blue points are long-duration simulations from the Tq series. A solid blue line at $\eta_{sim} = \eta_{fit}(100M_\odot)$ is shown to guide the eye. [An identical color scheme is adopted in the subsequent Figure 9.]

precisely on any theoretically anticipated correlation.

Even in the best of circumstances, we do not anticipate being able to accurately reproduce all parameters perfectly with our fitting process. At any mass, mass ratio, and spin, gravitational wave signals like $\psi_{4PB}(\lambda)$ with neighboring parameters λ closely resemble one another. Depending on the particular signal model and parameters λ , some parameter combinations are easier to identify than others via a fitting process. The easy-to-measure and hard-to-measure parameters can be identified via a Fisher matrix [34]; as an example, in the interpretation of low-mass nonprecessing binaries, a particular correlated combination of mass, mass ratio, and spin is exceptionally difficult to constrain observationally [34]. The accuracy of our fit is also limited by systematic differences between IMRPhenomB and our signal. In this proof-of-concept study we will not provide a detailed analysis of the systematic uncertainties associated with this fitting procedure.

B. High-mass limit

The late-time gravitational wave signal from a merging binary should be dominated by its leading-order quadrupole quasinormal mode, both in the simulation and corotating frame. On physical grounds, we therefore expect the best-fitting nonprecessing model to predict a similar final resonant frequency and decay timescale – or, equivalently, a similar final black hole mass M_f and spin a_f . As before, we will distinguish between the fi-

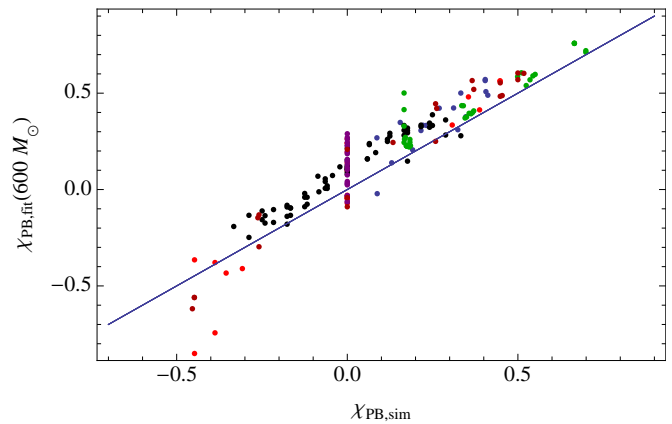


FIG. 9: **Low mass limit: Recovering the effective spin:** At low masses and therefore early times, the best-fit corotating-frame model reflects the initial binary. These panels show comparisons between the best-fit IMRPhenomB parameter χ_{eff} and χ_{PB} [Eq. (9)], using best-fit values at $M = 300M_\odot$. Colors indicate the Sq series (black); the Tq series (blue); and the T series (red). Colors indicate the Sq series (black); precessing binaries in the Tq series (blue); aligned spin binaries from the Tq series (green); and the short simulations of the T series (red), Eq series (purple), and Lq series (dark red). A solid blue line at $\chi_{PB,sim} = \chi_{PB,fit}(100M_\odot)$ is shown to guide the eye. Though provided at high mass ($M = 300M_\odot$) to insure short simulations are well-resolved, a similar distribution is recovered when using earlier epochs of longer signals (i.e., $M \simeq 100M_\odot$).

nal black hole mass and spins derived from our simulations ($M_{f,sim}, a_{f,sim}$) and derived from the best-fitting IMRPhenomB parameters ($M_{f,fit}, a_{f,fit}$).

The IMRPhenomB parameters χ_{sim}, η_{sim} are not transparently related to the final quasinormal mode frequencies and hence to the assumed final black hole mass and spin. To transform the best-fitting parameters $\eta_{fit}, \chi_{PB,fit}$ into a specific final black hole mass $M_{f,fit}$ and spin $a_{f,fit}$, we adopt relationships between the “initial” and post-merger state that reproduce the correlations seen in our simulations.

The transformation from nonprecessing binaries to final black holes is degenerate: the initial state is specified by three parameters (mass, mass ratio, and at least one “typical” spin¹⁰) while the final black hole has only two (mass and spin). Expressions exist which relate the pre- and post-merger parameters [11, 35–39, 39]. For generic binaries, because spins precess between forma-

¹⁰ Physically, a nonprecessing binary has *four* parameters: mass, mass ratio, and *two* spins. Due to symmetry, a nonprecessing binary’s $\psi_{42,2}$ must be reflection- and exchange-symmetric, implying it cannot trivially (e.g., linearly) depend on an antisymmetric combination of the binary’s spins. To an excellent approximation, the leading order quadrupole ($\psi_{42,2}$) produced by a nonprecessing binary depends on only *three* parameters: mass, mass ratio, and an effective spin.

tion and merger, the precise relationship between the pre- and post-merger state depends on precisely when the initial binary's parameters are specified [35, 40, 41]. In this work, however, these approximate analytic relationships will only be applied to nonprecessing initial parameters.¹¹ In that case, the final black hole mass can be estimated using the following combination the pre-merger mass, mass ratio, and spins using [39]

$$\frac{E_{\text{rad}}}{M} = 1 - M_f/M = [1 - E_{\text{ISCO}}(\bar{a})]\nu \quad (11a)$$

$$+ 4\nu^2[4p_o + 16p_1\bar{a}(\bar{a} + 1) + E_{\text{isco}}(\bar{a}) - 1] \quad (11b)$$

$$E_{\text{ISCO}} = \sqrt{1 - 2/3r_{\text{ISCO}}(a)} \quad (11c)$$

$$\bar{a} \equiv \frac{\hat{L} \cdot (S_1 + S_2)}{M^2} \quad (11d)$$

$$(p_o, p_1) \simeq (0.04827, 0.01707) \quad (11e)$$

where $r_{\text{ISCO}}(a)$ is the (dimensionless) radius of the Kerr horizon in Boyer-Lindquist coordinates. This approximation assumes the final black hole mass can depend on the spins only through \bar{a} – specifically, only through the total spin, projected along the orbital angular momentum; other approximations allow for more degrees of freedom and physics [11]. Similarly, the final black hole *dimensionless spin* can be computed from the pre-merger mass, mass ratio, and spins using either Eqs. (6-7) from Lousto et al. [11]¹² or the simpler Eq. (6) from [42]:

$$a_f \equiv J_f/M_f^2 = \frac{|\vec{a}_1 + \vec{a}_2 q^2 + \hat{L}|\ell|q|}{(1 + q^2)^2} \quad (12a)$$

$$|\ell| = 2\sqrt{3} + t_2\eta + t_3\eta + \frac{s_4|\vec{a}_1 + \vec{a}_2 q^2|^2}{(1 + q^2)^2} + \frac{s_5\eta + t_o + 2}{1 + q^2} \hat{L} \cdot (\vec{a}_1 + q^2 \vec{a}_2) \quad (12b)$$

$$(t_o, t_3, t_2) = (-2.89, 2.57, -3.52) \quad (12c)$$

$$(s_4, s_t) = (-0.1229, 0.45) \quad (12d)$$

These expressions accurately reproduce the results of our nonprecessing simulations. For example, given the initial spins, these expressions reliably reproduce the final black hole mass we derive from the final horizon to significantly better than 1% in all well-resolved simulations.

¹¹ The expressions provided in the text have been extremely accurately tuned for aligned-spin binaries. Though significantly less accurate for precessing binaries, these expressions are a qualitatively consistent relationship between our simulations' initial and final states when the binary has two precessing spins. In particular, these expressions usually predict the final black hole mass $M_{f,\text{sim}}/M_{\text{sim}}$ for generic precessing binaries to well within 1% of their true value. This scale can be helpfully compared with the significant scatter visible in the top panel of in Figure 10.

¹² To implement this expression exactly requires knowledge of the spins just prior to plunge and merger. We only apply this expression to nonprecessing systems – in fact, only to the **IMRPhenomB** best-fit parameters.

In terms of these relationships, we derive the final black hole mass and spin implied by the best-fitting **IMRPhenomB** parameters $M_{\text{fit}}, \chi_{\text{PB,fit}}, \eta_{\text{fit}}$ by direct substitution. For example, we evaluate the final black hole mass $M_{f,\text{fit}}$ by assuming $S_1 = \chi_{\text{PB,fit}} m_1^2 \hat{L}$ and $S_2 = \chi_{\text{PB,fit}} m_2^2 \hat{L}$, where $m_{1,2}$ are derived from η_{fit} , in the expression above:

$$M_{f,\text{fit}}/M_{\text{fit}} = 1 - \eta_{\text{fit}}(1 - E_{\text{ISCO}})(\bar{a}) \quad (13)$$

As shown by example in Figure 10, the best-fit parameters $M_{f,\text{fit}}, a_{f,\text{fit}}$ should be close to the final black hole's state. This figure compares the final black hole state identified in each simulation with the final state implied by the best-fitting **IMRPhenomB** parameters. At the late times and high masses studied here, both the signal model and **IMRPhenomB** will be dominated by late-time quasinormal mode decay, with some characteristic frequency $\omega_{2,2}(M_f, a_f)$. Qualitatively speaking, we expect the fitting process enforces near-equality between $\omega_{2,2}$ derived from ψ_{4PB} and the late time ringdown frequency in the corotating frame. The functional dependence of $\omega_{2,2}$ on M_f, a_f determines the key features seen in Figure 10. First, the mass ratio $\text{Im}\omega_{2,2}/\text{Re}\omega_{2,2}$ depends strongly on the final black hole spin a_f ; and, therefore, this fitting procedure should reliably determine the final black hole spin parameter; see, for example, the bottom panel in Figure 10. Second, because of the extremely limited number of cycles available to constrain the final black hole's properties, the total black hole mass cannot be reliably measured.¹³ In particular, because relatively little mass is lost to infinity ($M_f/M \simeq 1$), the fraction of mass lost to infinity cannot be reliably determined; see the top panel of Figure 10.

Above and beyond the fundamental limitations set by the functional form of $\omega_{2,2}$, the best-fit **IMRPhenomB** final spin differs systematically from the physical spin parameter for three reasons. Systematic differences exist between the **IMRPhenomB** model and our simulations, even for aligned spins; see the red curves in Figure 1. These differences arise due principally due to physical differences between the **IMRPhenomB** model and our merger simulations.¹⁴ In addition, the **IMRPhenomB** approximation uses its own implicit relationship between initial binary and final black hole, encoded in the final ringdown frequency [10]. As indicated in Figure 10 using red points, comparable differences between the physical final state and a final state derived from the best-fit **IMRPhenomB** model appear when this procedure is applied

¹³ A more detailed treatment of parameter estimation uncertainties in the ringdown signal is beyond the scope of this paper.

¹⁴ We have simulated identical nonprecessing systems at different resolutions and compared them with **IMRPhenomB**; all results for these simulations are included in Figure 1. The best-fit match and recovered parameters depends only weakly on resolution; by contrast, significant differences exist between **IMRPhenomB** and any of our models.

both to precessing and nonprecessing binaries. We have eliminated physical degrees of freedom and introduced systematic error by requiring the final black hole mass and spin depend only on the black hole spins through χ_{PB} . By comparison, neither expressions we use to relate the initial and final state [Eqs. (11, 12)] depend on spins through χ_{PB} ! Instead, both expressions used here depend on the total spin $\mathbf{S}_1 + \mathbf{S}_2$. Alternatively, Table I has several examples of simulations with identical mass ratio and χ_{PB} but producing significantly different a_f ; see, for example, Sq(4,0.6,90) and Sq(4,0.6,270). Finally, the corotating-frame transformation involves a rotation at an appreciable proportion of the final black hole's quasinormal mode frequency [14]. As a result, we fully expect the best-fit parameters to be offset from the physical parameters of the final black hole.

V. SYNTHETIC SIGNALS AND MISSING PHYSICS

A. Synthetic signals

As described in previous work on corotating frames [18–21], the similarity between corotating-frame modes and nonprecessing systems suggests a simple strategy for synthetic waveform generation. In this procedure, we join some nonprecessing set of modes $\psi_{4l,m}^{ROT}$ to a time-dependent rotation \hat{R} , constructively generating a synthetic waveform for each line of sight. For example, each of the corotating-frame modes could be interpolated phenomenologically, starting with our collection of corotating-frame modes. Likewise, prior to merger the rotation operation could track expected trajectory based on adiabatic quasicircular spin-orbit evolution; after merger, the rotation operation could be measured and calibrated to mimic suitable precession. This very aggressive strategy requires careful, complicated interpolations: each mode and spins depends on several parameters (two masses and two spin vectors). Less aggressive strategies could adopt simpler models for precession or the inspiral signal. For example, a well-motivated, parameterized inspiral-merger-ringdown model like the effective-one-body model could track the orbital phase.

To assess how well this strategy could perform in optimal circumstances, we assume the physical rotation and best-fitting IMRPhenomB can be determined for each candidate physical system. In this most optimistic case, the match $P_{\max,\text{sim}}$ [Eq. (1)] quantifies the degree of similarity between the simulation-frame (2,2) mode $\psi_{4NR,2,2}$ and the (2,2) mode generated by this synthetic procedure: $[R^{-1}\psi_{4PB}(\lambda_{PB})]_{2,2}$. The top panel of Figure 3 shows the distribution of $P_{\max,\text{corot}}$. In short, this strategy will be strikingly successful, fitting the IMR signal from our generic mergers to better than a few percent.

More striking still, our simulations generally show $P_{\max,\text{corot}} \simeq P_{\max,\text{sim}}$. In other words, we only needed to assess how similar the corotating-frame signal is to

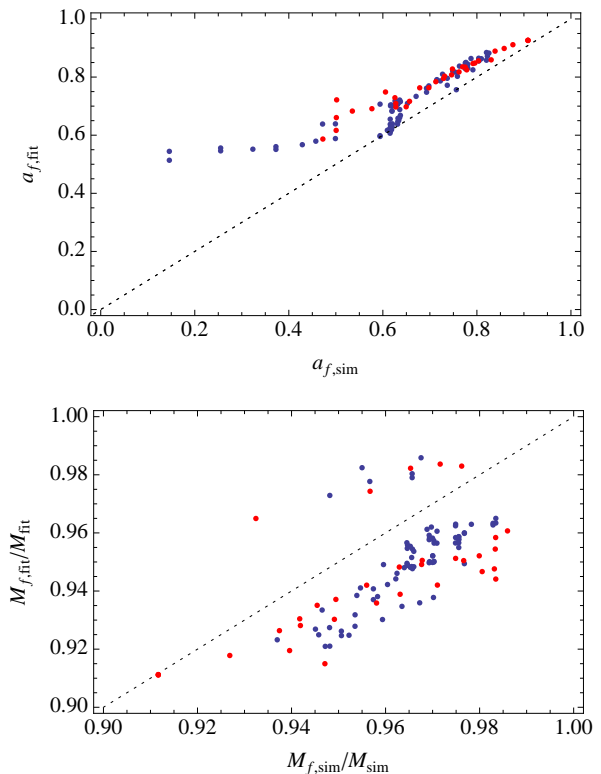


FIG. 10: High mass: Best fit approximately recovers the final state: At $M \simeq 1000M_\odot$, a scatter plot of the true ($M_{\text{sim}}, a_{\text{sim}}$) and best-fit ($M_{\text{fit}}, a_{\text{fit}}$) final black hole masses (bottom panel) and spins (top panel), derived from our precessing simulations (blue) and nonprecessing simulations (red). The best-fit final black hole properties are derived from the IMRPhenomB best-fit parameters using Eqs. (11,12). In both figures, a dotted black line is provided to guide the eye onto $a_{f,\text{sim}} = a_{f,\text{fit}}$ and similarly. Because the IMRPhenomB model claims to reproduce nonprecessing binaries, the distribution of the red points can be used to estimate systematic uncertainties in this method. For example, in the top panel, the systematic offset between the red points and the line $a_{f,\text{sim}} = a_{f,\text{fit}}$ suggests significant systematic differences between our simulations' ringdown frequencies and the model of IMRPhenomB. In the bottom panel, the significant scatter in both red and blue points reflects our inability to measure total masses to better than a few percent by a fitting procedure; see also the bottom panel in Figure 2. This figure includes a separate point for each individual simulation, including some simulations with physically identical parameters but performed with different resolutions. To better resolve the final black hole quasinormal modes, we have explicitly excluded all simulations performed with $h = M/77$.

a nonprecessing signal model, to determine how well a synthetic precessing search will perform.

Serious challenges exist before this synthetic waveform can be implemented in practice. For example, the relationship between the physical parameters of the binary, the physical rotation versus time, and the best-fitting nonprecessing model parameters must be carefully tabulated before these synthetic signals could be applied to

parameter estimation. Also, this model omits physical degrees of freedom and cannot reproduce the signal perfectly, even with the best-possible nonprecessing signal model. As a practical matter, the latter limit sets the accuracy to which this program should be pursued in detail.

Our study also allows us to better understand the essential features a more complete interpolation strategy must have. Because the best-fitting nonprecessing systems are different at low and high mass, a robust strategy must produce waveforms that resemble different nonprecessing systems early and late in the signal. This procedure could work physically, with a well-motivated IMR model; somewhat phenomenologically, using two basis epochs and interpolating the junction conditions versus spins; or completely phenomenologically, interpolating the whole waveform.

B. Limitations of nonprecessing analogs and synthetic precessing waveforms

Precessing binaries break a symmetry: reflection through the orbital plane. As a result, precessing binaries have waveforms with fundamentally more complexity, *even in the corotating frame*. No nonprecessing waveform, no matter how rotated, can reproduce that symmetry breaking; see Appendices A 4 and A 3. As a result, the straightforward approach described above has limited accuracy, applied to generic precessing systems; see the executive summary and Figure 3. In this section, we describe the physics missed when one assumes the corotating-frame waveform has an instantaneous reflection symmetry.

The straightforward approach described above has not included the *direct* feedback of precessing spins on the waveform. For example, during the inspiral the orbiting spins source current quadrupole radiation. By breaking reflection symmetry about the instantaneous orbital plane, the current quadrupole and similar precession-sourced terms introduce behavior which cannot be reproduced by nonprecessing waveforms, no matter how rotated. As described in detail in the executive summary, Figure 5 shows the reflection-symmetric and reflection-asymmetric parts of the $l = 2$ corotating-frame waveform, illustrating the small but increasingly important impact of symmetry-breaking terms. Prior to merger, the symmetry-breaking terms are small, typically several PN orders smaller than the dominant term for each mode; see Appendix A 4 for a symmetry decomposition of the PN expansion. During and after merger, however, these symmetry-breaking terms become a significant fraction of the overall amplitude $|\psi_4|$. These symmetry-breaking terms reflect an instantaneous bias towards preferentially left- or right-handed emission [14]. In Figure 5 as in most cases, the dominant asymmetry occurs between the $(2, \pm 2)$ modes.

The effect of precessing spins and bias towards one he-

licity or another is far from academic, particularly at high mass. Using a data-analysis-motivated comparison in the *simulation frame*, O’Shaughnessy et al. [14] have already showed that this oscillating bias towards one handedness or the other leads to a preferred handedness in the detected signal, changing slowly as a function of mass and line of sight. These modulations distort the $2, 2$ mode and generally cannot be perfectly reproduced by a nonprecessing waveform. Figure 5 and comparable calculations for generic sources suggests that strong (tens of percent) symmetry breaking occurs ubiquitously in precessing mergers.

The synthetic procedure described above also neglects higher harmonics. Higher harmonics are well-known to produce observationally-accessible modulations of the gravitational wave signal along generic lines of sight for generic high-mass mergers [25, 26]. As suggested by Figure 5, higher harmonics are *at least* as important as (and difficult to disentangle from) spin precession effects. Our calculations support previous results suggesting that the observationally-accessible information requires detailed models for several harmonics, beyond the leading order [25, 26].

Our results, along with the previously mentioned helicity bias described in [14], strongly suggest that high-mass precessing binaries cannot be well-understood without breaking reflection symmetry through the orbital plane. In turn, these symmetry-breaking terms cannot be understood without modeling transverse spin dependence in detail. For strongly precessing asymmetric binaries, we do not believe the waveform generation problem cannot be completely decoupled from kinematics, at an observationally relevant level. Finally, as in previous studies, we anticipate higher harmonics will be required to interpret the merger signal from generic precessing sources.

VI. CONCLUSIONS

In this paper we explore a simple “synthetic” model for the leading-order gravitational wave signal from precessing, merging binaries: a suitable nonprecessing binary, viewed in a suitable noninertial frame. Using a data-analysis-driven diagnostic, we compare the $(2, 2)$ modes extracted from a large collection of binary black hole merger simulations to such a synthetic model, both in an inertial frame and a “corotating” frame which tracks the evolution of the binary. In all cases explored here, we find that the late-time inspiral and merger signal from generic black hole mergers can be reasonably approximated by a nonprecessing binary seen in a corotating frame. Moreover, as expected on physical grounds, at early times the corotating-frame signal resembles emission from a nonprecessing binary with physically similar parameters: similar mass, mass ratio, and “effective spin.” Our study restricted attention to our numerical simulations, without analytic extrapolations at early (“hybridization”) or late times; that said, our results suggest that followup in-

vestigations with suitable semi-analytic hybrids can reasonably approximate generic precessing merger signals for all time.

Though this approximation neglects significant physics and has correspondingly limited accuracy, this “synthetic” approach allows the efficient generation of complicated, multimodal signals from generic merging sources. Because this procedure bootstraps experience gained from nonprecessing sources, we strongly recommend more effort be devoted to modeling, approximating, or hybridizing the observationally-relevant higher harmonics from generic two-spin nonprecessing binaries; to modeling precession before, during, and after merger; and hence to generating qualitatively realistic synthetic precessing merger signals.

While a qualitatively adequate zeroth approximation, this procedure does not easily generalize to a high-precision quantitative approximation, with controlled error estimates. Nonprecessing waveforms simply cannot self-consistently reproduce features tied to the system’s *kinematics*: the orbital phase versus time; the ringdown mode frequencies, set by the final black hole’s mass and spin; the ringdown mode amplitudes, which can reflect spin-orbit misalignment; et cetera. As a familiar example, in post-Newtonian calculations, time-dependent spin-orbit and spin-spin terms must be included in the orbital phase and calculated from suitable spin precession equations. More significantly, nonprecessing waveforms have a *reflection symmetry* and thus cannot reproduce current quadrupole or similar asymmetric radiation modes. Our study emphasized reproducing the principal $l = 2$ emission from merging binaries; generic asymmetric precessing systems possess several strong higher harmonics, many of which must be included to accurately reproduce even a nonprecessing source [25]. Our calculations support previous results suggesting that the observationally-accessible information requires detailed models for several harmonics, beyond the leading order [25, 26]. We anticipate detailed parameter estimation of high-mass ($M > 100M_\odot$) binary mergers will require detailed modeling of multiple modes of generically precessing binaries, an effort in support of which a considerably larger sample of generic binary mergers are required. Moreover, because of the significant role the merger plays in comparable-mass binary black hole mergers with $M \gtrsim 20M_\odot$, we suspect that high-precision parameter estimation of generic precessing low-mass systems will also require a model for precession during merger that has been carefully calibrated against numerical simulations.

To the best of our knowledge, gravitational wave detection strategies have never been tested against generic merger signals that self-consistently include precession and ringdown. Based on the quantitative similarities characterized in this work, we strongly recommend that gravitational wave data analysis strategies for high-mass binaries ($M > 50M_\odot$) be tested against simple synthetic precessing inspiral-merger-ringdown waveforms, gener-

ated by combining plausible rotations and nonprecessing binary merger signals.

Appendix A: Mathematical methods

1. Extracting the corotating waveform

Particularly early in the inspiral, the gravitational wave signal from merging binaries can be approximated by the emission from instantaneously nonprecessing binaries, slowly rotated with time as the orbital plane precesses [18, 23, 43]. At late times, the gravitational wave signal will reflect perturbations of a single black hole with a well-identified spin axis. In both cases and in between, a well-chosen instantaneous or global frame can dramatically simplify the decomposition of $\psi_4(\hat{n}, t)$ in terms of spin-weighted harmonic functions $\psi_{4lm}(t)$. These simplifications make it easier to distinguish physically relevant from superfluous modulations; to model emission and generate hybrids; and to formulate tests of general relativity itself.

In this paper, we adopt a preferred direction \hat{V} aligned with the principal axes of $\langle \mathcal{L}_a \mathcal{L}_b \rangle$ [19]. The tensor $\langle \mathcal{L}_a \mathcal{L}_b \rangle$ is defined by the following angular integral, acting on a symmetric tensor constructed from the rotation group generators \mathcal{L}_a acting on the asymptotic Weyl scalar:

$$\begin{aligned} \langle \mathcal{L}_a \mathcal{L}_b \rangle &\equiv \frac{\int d\Omega \psi_4^*(t) \mathcal{L}_a \mathcal{L}_b \psi_4(t)}{\int d\Omega |\psi_4|^2} \\ &= \frac{\sum_{lm m'} \psi_{4lm}^* \psi_{4lm'} \langle lm' | \mathcal{L}_a \mathcal{L}_b | lm \rangle}{\int d\Omega |\psi_4|^2} \end{aligned} \quad (\text{A1})$$

where in the second line we expand $\psi_4 = \sum_{lm} \psi_{4lm}(t) Y_{lm}^{(-2)}(\theta, \phi)$ and perform the angular integral. The action of the rotation group generators \mathcal{L}_a on basis states $|lm\rangle$ is well-understood, allowing us to re-express the tensor $\langle \mathcal{L}_a \mathcal{L}_b \rangle$ as [44]:

$$\begin{aligned} I_2 &\equiv \frac{1}{2} (\psi, L_+ L_+ \psi) \\ &= \frac{1}{2} \sum_{l,m} c_{l,m} c_{l,m+1} \psi_{l,m+2}^* \psi_{l,m} \end{aligned} \quad (\text{A2a})$$

$$\begin{aligned} I_1 &\equiv (\psi, L_+ (L_z + 1/2) \psi) \\ &= \sum_{l,m} c_{l,m} (m + 1/2) \psi_{l,m+1}^* \psi_{l,m} \end{aligned} \quad (\text{A2b})$$

$$\begin{aligned} I_0 &\equiv \frac{1}{2} (\psi | L^2 - L_z^2 | \psi) \\ &= \frac{1}{2} \sum_{l,m} [l(l+1) - m^2] |\psi_{l,m}|^2 \end{aligned} \quad (\text{A2c})$$

$$I_{zz} \equiv (\psi, L_z L_z \psi) = \sum_{l,m} m^2 |\psi_{l,m}|^2 \quad (\text{A2d})$$

where $c_{l,m} = \sqrt{l(l+1) - m(m+1)}$. In terms of these

expressions, the orientation-averaged tensor is

$$\langle \mathcal{L}_a \mathcal{L}_b \rangle = \frac{1}{\sum_{l,m} |\psi_{l,m}|^2} \begin{bmatrix} I_0 + \text{Re}(I_2) & \text{Im}I_2 & \text{Re}I_1 \\ & I_0 - \text{Re}(I_2) & \text{Im}I_1 \\ & & I_{zz} \end{bmatrix} \quad (\text{A2e})$$

The dominant eigendirection \hat{V} of this tensor specifies two of the three Euler angles needed to specify a frame:

$$\hat{V} = (\cos \alpha \sin \beta, \sin \alpha \sin \beta, \cos \beta). \quad (\text{A3})$$

To determine the remaining Euler angle (γ), we self-consistently adjoin a rotation in the plane transverse to this orientation, to account for the gradual buildup of transverse phase due to precession [20]:

$$\gamma(t) = - \int_0^t \cos \beta \frac{d\alpha}{dt} dt \quad (\text{A4})$$

Having specified the three Euler angles that define a new frame, we rotate the simulation-frame $Y_{l,m}^{(-2)}$ coefficients of ψ_4 to the new, time-dependent frame:

$$\psi_{4l,m}^{ROT} = \sum_{\bar{m}} D_{m\bar{m}}^l(R(\alpha, \beta, \gamma)^{-1}) \psi_{4l\bar{m}} \quad (\text{A5})$$

$$= \sum_{\bar{m}} e^{i\bar{m}\gamma} d_{\bar{m}m}(\beta) e^{im\alpha} \psi_{4l\bar{m}} \quad (\text{A6})$$

where $R(\alpha, \beta, \gamma)$ carries the \hat{z} axis to \hat{V} , plus a rotation transverse to that direction by γ .

All simulations of the same physical system (with the same tetrad normalization) will agree on $\psi_4(t, \hat{n})$. The choice of frame at future infinity reparameterizes the same results. While our choice for the preferred frame continues to precess during and after merger, to the extent our simulations have so far resolved, other authors' preferred frames may converge to a fixed frame, aligned with the final total angular momentum direction \hat{J}_f . The choice of corotating frame depends on convention [44]. As a result, the corotating-frame waveforms we describe below can differ from those extracted using other conventions, with differences increasing at late times. For the purposes of this paper – comparison with nonprecessing binaries, principally of the leading-order mode – we anticipate these differences are small.

As shown in prior work [14] and illustrated again in the bottom panel of Figure 11, the preferred orientation \hat{V} and rotation γ evolve smoothly, usually precessing around the total angular momentum direction. In this work, we do not construct synthetic waveforms and therefore do not report on a functional approximation to the Euler angles as a function of time. That said, using a frame aligned with the (initial) total angular momentum \mathbf{J} to define the Euler angles, the opening angle β is nearly constant; the precession angle α evolves steadily forward, at a precession rate set either by spin-orbit coupling (in the inspiral) or the final quasinormal mode frequencies (during ringdown); see Figure 8 in [14]. We therefore expect the rotation $R(t)$ can be easily and reliably fit as a function of time.

2. Complex overlap and mass-weighted comparisons

We coherently compare the (noise-free) signal expected along any pair of orientations with a complex inner product motivated by the detector's noise power spectrum [19, 26]. For our purposes, numerical relativity simulations take as inputs binary black hole parameters and desired line of sight (denoted by λ) and return the Weyl scalar $\psi_4(t)$, a complex-valued function of time evaluated along that line of sight. For any pair of simulations and lines of sight, we compare ψ_4 and ψ_4' by a complex overlap

$$P(\lambda, \lambda') \equiv \frac{(r\psi_4 | r\psi_4')}{|r\psi_4| |r\psi_4'|} \quad (\text{A7a})$$

$$(A, B) \equiv \int_{-\infty}^{\infty} 2 \frac{df}{(2\pi f)^4 S_h} \tilde{A}(f)^* \tilde{B}(f) \quad (\text{A7b})$$

where S_h is a detector strain noise power spectrum. In this and subsequent expressions we used unprimed and primed variables to distinguish between the two waveforms being compared, involving potentially distinct parameters λ' and lines of sight \hat{n}' . For simplicity and to avoid ambiguity, in this paper, we adopt a semi-analytic model for the initial LIGO sensitivity [45]. As with the single-detector overlap, the complex overlap can be maximized over the event time and *polarization* (t_c, ψ_c) and by a simple Fourier transform:

$$P_{max} \equiv \max_{t_c, \psi_c} |P| \quad (\text{A8})$$

$$= \frac{1}{|\psi_4| |\psi_4'|} \left| \int_{-\infty}^{\infty} 2 \frac{df}{(2\pi f)^4 S_h} \tilde{\psi}_4(f)^* \tilde{\psi}_4'(f) e^{i(2\pi f t_c + \psi_c)} \right|$$

The overlap P_{max} is unity for identical simulations and lines of sight. How different must P_{max} be from 1 to be significant? Roughly speaking, mismatch leads to detectable effects when $1 - P > 1/\rho^2$ [27], for ρ the signal amplitude. Given the expected signal amplitudes for the first few gravitational wave events, a nonprecessing analog is for practical purposes indistinguishable from a corotating waveform with $P_{max} > 99\%$.

Unlike other authors, in this paper we only employ waveforms extracted from the fully simulated spacetime, without making any attempt to hybridize that signal onto a post-Newtonian precursor. At the same time, we adopt a data-analysis-driven comparison, driven by the unique bandpass of a plausible detector. This comparison requires us to adopt *physical* timescales ($\propto M$) and frequency scales ($\propto 1/M$). Because the simulation has finite duration and dynamics with a finite frequency range, our simulations are physically relevant only for a specific range of masses. The limit at the low mass end is set by the simulations' initial orbital frequency, which at very low masses ($\simeq 100M_\odot$) can lie in a detector's sensitive band. At the high mass end, the exponential decay of post-merger oscillations implies that our comparisons are contaminated by numerical noise at above $\simeq 1000M_\odot$.

To determine these two limits unambiguously, we perform the following quantitative tests. To set the upper mass limit, we use a one-parameter family of simulations k similar to Sq(4, 0.6, 270, 9), performed at different resolutions. We require the overlap $\langle \psi_{42,2,k} | \psi_{42,2,k'} \rangle / \| \psi_{42,2,k} \| \| \psi_{42,2,k'} \|$ be greater than 0.97 for *all* pairs of resolutions. The largest mass for which this bound holds is $\simeq 700M_\odot$. To set the lower mass limit, we explored how the overlap between a signal and a truncated copy of itself changed, depending on how much of the early inspiral was removed; see Appendix B 2 and Figure 11. To conservatively insure the signal duration had less than a 1% influence on the overlap, we extremely conservatively limited $M > 400M_\odot$ for our typical short-duration signals ($r_{\text{start}} = 6.2M$).

Advanced detectors can nominally be sensitive to *extremely* high-mass objects $M > 500M_\odot$, if frequencies below 40 Hz are properly calibrated. In the text, we have optimistically assumed all frequencies above 5 Hz will be calibrated, allowing ground-based interferometers to detect and measure the properties of binaries with total masses up to $\simeq 2500M_\odot$. Realistically, however, ultra-low-frequency detector noise and calibration remains a significant challenge, owing to the complicated and historically nongaussian noise in this regime [46]. Given the suspension and other realistic constraints, advanced detectors may be calibrated only for frequencies above 10 Hz, limiting gravitational wave detection to $\lesssim 1500M_\odot$.

3. How many degrees of freedom are eliminated in going to a corotating frame?

At each time step, the corotating frame expansion uses the extracted waveform data to reconstruct 3 Euler angles. Two of the three Euler angles, specifying the direction of \hat{V} , are reconstructed from the instantaneous value of $\langle \mathcal{L}_a \mathcal{L}_b \rangle$ and do not depend on the past history of the binary.¹⁵ The third Euler depends weakly on the past history of the binary, through the minimal-rotation condition. By contrast, each constant- l subspace has $2 \times (2l + 1)$ real degrees of freedom in the amplitudes and phases of its $(2l + 1)$ modes. For example, the $l = 2$ subspace alone has 10 real degrees of freedom, while the set of modes $l \leq 4$ has 42. By simple parameter counting, a corotating frame expansion cannot eliminate as many degrees of freedom as can exist in the waveform.

By contrast, nonprecessing simulations exhibit many extremely strong symmetries between different modes. First, nonprecessing modes are always *chiral*:

$$\tilde{\psi}_{4l,m}(f) = 0 \quad \text{m f} < 0 \quad (\text{A9})$$

¹⁵ Since the orientation tensor $\langle \mathcal{L}_a \mathcal{L}_b \rangle$ cannot distinguish between $\pm V$, we additionally require \hat{V} be continuous and start with $\hat{V} \cdot \hat{L} > 0$.

Second, nonprecessing binaries have amplitude and phase conjugation symmetry: $\psi_{4l,m}^* = (-1)^l \psi_{4l,-m}$. Third, during the inspiral, all modes evolve in phase, with $\arg \psi_{4l,m} = m\Phi_{\text{orb}}$. Repeatedly corroborated empirically [47], this fact suggests that the inspiralling binary emits as if a rigid body. These symmetries significantly reduce the number of degrees of freedom needed to specify a nonprecessing source. To use the $l = 2$ subspace as an example and omitting the three (constant) Euler angles needed to describe the system, prior to merger only one phase and 3 amplitudes are needed to describe the system, while after merger, 2 phases and three amplitudes are needed.

Our corotating expansion does not impose any of these properties. As a concrete example, consider a fictitious source producing only (2, 2) and (2, -2) modes in some constant frame misaligned with the global reference frame. This source can produce each mode independently, with arbitrary amplitude and (chiral but otherwise arbitrary) phase as a function of time. Our corotating expansion would identify the (constant) orientation of that frame and the (arbitrary) functional form of the two basis sources.

That said, a phase-conjugate “corotating” signal ($\psi_{4l,m} = (-1)^l \psi_{4l,-m}^* = a_{l,m}$) plus an arbitrary time-dependent rotation has enough parameters to fit *many but not all* sources. Counting parameters, a phase-conjugate source would have $l + 1$ amplitudes and l phases in each constant- l subspace. Including an arbitrary rotation lets a phase-conjugate source fit $2l + 4$ degrees of freedom. For the $l = 2$ subspace, however, two degrees of freedom remain that this form, though relatively generic, cannot fit: the two conjugate-*antisymmetric* (“odd”) moments ($\psi_{4l,m} = -(-1)^l \psi_{4l,-m}^* = b_{lm}$ for $m = 1, 2$). More generally, a phase-conjugate corotating source will never fit the odd moments $b_{l,m}$ in each constant- l subspace. Additionally, even a phase-conjugate source can conceivably fit *different orientations to each constant- l subspace*.

To conclude, nonprecessing simulations exhibit many strong symmetries. While we *hope* any “nonprecessing analog” will satisfy them, our corotating frame will not enforce them. First, each constant- l subspace has a consistent preferred direction at each time. Second, prior to merger, the corotating modes have common phase evolution. Finally, nonprecessing systems cannot source current moments and must emit symmetrically when reflected through the orbital plane.

4. Symmetry expansions in the corotating frame

To better identify and discuss small features that spin precession introduces into the waveform, we sometimes separate the *corotating-frame* Weyl scalar $R^{-1}\psi_4$ into different parts, reflecting symmetries.

One way to split ψ_4 is the usual ($l + 1$ derivatives of the) “mass” and “current” quadrupole moments $\mathcal{I}_{l,m}$ and

$\mathcal{S}_{l,m}$ respectively, which we define as [48, 49]

$$\psi_{4l,m} = -\frac{1}{\sqrt{2}rM}[\mathcal{I}_{l,m} - i\mathcal{S}_{l,m}] \quad (\text{A10})$$

where $\mathcal{I}_{l,m} = (-1)^m \mathcal{I}_{l,-m}^*$ and $\mathcal{S}_{l,m} = (-1)^m \mathcal{S}_{l,-m}^*$ have the usual symmetry [48]. This operation defines two projections $\psi_4 = \psi_4^M + \psi_4^S$ that uniquely separate ψ_4 into mass and current contributions.

Unfortunately, even the leading-order emission from nonspinning binaries produces both mass and current moments [23, 48, 49]. The standard mass and current decomposition does not provide a high-precision tool to distinguish between the nonprecessing and precession-only contributions.

For our phenomenological purposes, a more productive decomposition uses classical axial and polar parity. For notational convenience, we define this split on a mode-by-mode basis, using conjugation symmetry to define CP-odd ($b_{l,m} = -(-1)^l b_{l,-m}^*$) and CP-even ($a_{l,m} = (-1)^l a_{l,-m}^*$) parts of the corotating-frame $R^{-1}\psi_4$, as described in the text [Eq. (3)]. As a concrete example, we provide leading-order post-Newtonian expressions for $h_{l,m}$ below.

Nonprecessing binaries are *even* under this transformation, radiating symmetrically above and below their orbital plane. Equivalently, on a mode-by-mode basis, each R-handed mode $m > 0$ has a corresponding L-handed mode $m < 0$ that radiates identically but in the opposite direction. Precessing binaries break this symmetry, even in the corotating frame. As noted in [14], precessing binaries show a slight bias towards either R- or L-handed emission at any instant, with the sign of the bias oscillating as the orbit changes the relative orientation of the spins to the binary separation. This symmetry-breaking bias generally persists in the corotating frame on a mode-by-mode basis: often $b_{l,m} \neq 0$. For this reason, a conjugation-symmetry-based diagnostic provides a powerful tool to identify and quantify the impact of precessing spins in a corotating frame.

To illustrate the expected functional form and symmetry properties of different multipole orders, we provide selected terms from the a, b symmetry decomposition of $h_{l,m}$, as tabulated elsewhere [23]. To highlight their symmetry properties, we convert their notation to explicit Cartesian 3-vector operations. Specifically, in place of the orbital phase (including tail terms) Ψ , we adopt a coordinate 3-vector \hat{r} for the radial separation. To convert between coordinate expressions and vectors, we employ a reference frame \hat{x}, \hat{y} that corotates with the binary¹⁶

$$\hat{e}_\pm \equiv \frac{\mp}{\sqrt{2}}(\hat{x} \pm i\hat{y}) \quad (\text{A11})$$

$$e^{i\Psi} \equiv -\sqrt{2}\hat{r} \cdot e_+^* \quad (\text{A12})$$

Our expressions follow directly from their expressions, substituting $\iota = 0$ and replacing powers of $\exp i\Psi$ with $\sqrt{2}\hat{r} \cdot e_+^*$ as needed.

For example, the leading-order $l = 2$ multipoles have the following form, highlighting spin dependence and working to v^4 order:

$$a_{2,2}^h = \text{spin-independent to } O(v^5) \quad (\text{A13})$$

$$b_{2,2}^h = \frac{M16\sqrt{\pi/5}}{d_L} v^4 \eta \mathcal{S}_a r_b (e_+ e_+)^{*ab} \quad (\text{A14})$$

$$a_{2,0}^h = \frac{4M\sqrt{2\pi/15}}{d_L} v^4 (-i\eta) (\hat{r} \times \mathcal{S}) \cdot \hat{L} \quad (\text{A15})$$

$$b_{2,0}^h = 0 \quad (\text{A16})$$

$$a_{2,1}^h = \hat{r} \cdot e_+^* \frac{M\sqrt{2\pi/5}}{d_L} \eta \left[\frac{8}{3} \delta v^3 - 4\mathcal{S} \cdot \hat{L} v^4 + O(v^5) \right] \quad (\text{A17})$$

$$b_{2,1}^h = O(v^5) \quad (\text{A18})$$

where to simplify comparisons with the literature we provide the symmetry coefficients a, b derived from the complex h (i.e., $\psi_4 = \partial_t^2 h = \partial_t^2 (a^h + b^h)$). In these expressions, we employ the same notation as [23]:

$$\eta \equiv \frac{m_1 m_2}{(m_1 + m_2)} \quad (\text{A19})$$

$$\delta \equiv \frac{m_1 - m_2}{m_1 + m_2} \quad (\text{A20})$$

$$\chi_\pm = (\mathbf{S}_1/m_1^2 \pm \mathbf{S}_2/m_2^2)/M \quad (\text{A21})$$

Additionally, following [44] we introduce

$$\begin{aligned} \mathcal{S} &= \chi_- + \delta \chi_+ \\ &= \frac{1}{M} \left(\frac{\mathbf{S}_1}{m_1} - \frac{\mathbf{S}_2}{m_2} \right) \end{aligned} \quad (\text{A22})$$

Appendix B: Simulations

1. Simulations

Table 1 in [14] enumerates many of the simulations and groups of simulations shown in this study; we adopt similar notation to characterize each simulation (T, Tq, S, Sq, ...). To simplify the process of identifying and distinguishing between similar simulations, we provide each simulation with a short descriptive string. While the specific interpretation of the string depends on the simulation type, many of our simulations are denoted by a string of the form $X(q, a, \theta, d)$ where q is the mass ratio; a is the typical dimensionless spin; θ is an angle; and d is the initial binary separation in units of M . Initial data was evolved with *Maya*, which was used in previous binary black hole (BBH) studies [50–58]. The grid structure for each run consisted of 10 levels of refinement provided by *CARPET* [59], a mesh refinement package for *CACTUS* [60]. Each successive level's resolution decreased

¹⁶ In the notation of [23], α would evolve with time.

by a factor of 2. Sixth-order spatial finite differencing was used with the BSSN equations implemented with Kranc [61]. While the initial data, grid size, resolution boundaries, and peak resolution all differ between simulation, each simulation a member of one of the following classes:

- **S series:** In this series, two equal-mass holes are positioned at $\pm 3.1M$, starting with $S_1/m_1^2 = -a\hat{x}$ and $a_2 = a\hat{n}(\theta, 0)$ for several choices of θ and a . The outer boundaries are located at $317.4M$. Each simulation was performed at a resolution of $M/77$ on the highest refinement level. Notably, one refinement region extends between $r = 20M$ to $r = 80M$. As previously [62], the outermost refinement levels from $r = 80M$ to $r = 317M$ are too low resolution ($dx > 3M$) to safely reproduce fine, high-frequency features in the waveform. We therefore extract on the refinement region bounded by $[20, 80]M$ (i.e., at $r = 40, 50, 60, 75$).
 - **T series:** In this series (also denoted the “A series” elsewhere), the two equal-mass holes are positioned at $\pm 3.1M$, starting with $S_1/m_1^2 = a\hat{z}$ and $S_2/m_2^2 = a\hat{n}(\theta, 0)$ for several choices of θ and a . The outer boundaries are at $317M$. Each simulation was performed at a resolution of $M/77$ on the highest refinement level. Refinement boundaries occur at $r = 40, 79M$, with $dx = 0.83M$ in that refinement region. As previously [62], we therefore extract on $r = 40, 50, 60, 75$.
 - **Sq series:** Dimensionless spin vectors \mathbf{S}_k/m_k^2 are chosen as in the S series. Each simulation was performed at a resolution of $M/140$ on the highest refinement level. As above, we extract only in one refinement region, here at $r = 40, \dots 90$. However, the grid size depended on the initial starting separation.
- For simulations started with initial separation $d = 9M$, the outer boundaries are at $307M$. Between $r = 32M$ and $r = 102M$, the refinement levels have $dx = 0.9M$.
- For simulations started with $d = 6.2M$, the outer boundaries are at $409M$. Between $r = 25M$ and $102M$, refinement levels have $dx = 0.9M$.
- **Tq series:** Dimensionless spin vectors \mathbf{S}_k/m_k^2 are chosen as in the T series. The outer boundaries are at $409.6M$. Each simulation was performed at a resolution of $M/120$ on the highest refinement level. Refinement boundaries occur at $r = 20, 102M$, between which $dx = 1M$. We extract in this refinement region along $r = 40, \dots 90$ and extrapolate to infinity in that zone.

When both spins are in the orbital plane ($\theta = \pi/2$ or $3\pi/2$), the initial data adopted for these series can be comparable to evolutions performed elsewhere. For example, the Sq(4,0.6,90) and

Tq(4,0.6,270) sequences are almost identical, modulo a small shift in initial separation.

- **V series:** In this series, the two equal-mass holes are positioned with a separation $d = 6.2$, starting with $S_1/m_1^2 = a\hat{n}(\theta, \phi)$ and $S_2/m_2^2 = a\hat{n}(\theta, \phi + \pi)$. The outer boundaries are at $317M$; the highest resolution is $M/77$; and we extract information in the refinement region between $20M \dots 80M$, in which $dx = 0.8M$.
- **Lq series:** Similar to the Sq series, except using a wider range for the smaller black hole’s spin direction. Each simulation was performed with a resolution $M/140$ on the highest refinement level; the simulation extends to $r = 409.6M$; we extract only in one refinement region between $40M \dots 102M$, where grid spacing is $dx = 0.9M$.
- **Eq series:** Similar to the Lq series, except starting at a larger separation ($d = 7M$) and both spins are in the xy plane and antiparallel, with $S_1/m_1^2 = 0.6\hat{n}(\pi/2, \phi)$. Resolutions and extraction radii are as described above.
- **z and zq (aligned) series:** Equal-mass (z) and unequal mass (zq) aligned-spin binaries, with identical specific angular momentum \mathbf{S}/m^2 on each black hole. The outer boundaries are at $317M$; most simulations have their finest level of refinement at $h = M/103$; and refinement boundaries occur at $r = 39M$ and $r = 79M$, between which $dx = 1.24M$.
- **zU (aligned, asymmetric):** Unequal-mass aligned-spin binaries, where the two black holes do not have identical specific angular momentum \mathbf{S}/m^2 . The outer boundaries are at $r = 409.6M$; each simulation’s finest refinement level has $h = M/160$; and in the interval $25 \dots 102.4M$, where we extract information, the grid spacing is $dx = 0.8M$.

Given the significant systematic errors inherent in any comparison between IMRPhenomB and numerical simulations, we did not extrapolate the waveform to infinity or in resolution. Instead, we performed calculations on a fixed resolution and fixed extraction radius. We used multiple resolutions and extraction radii to assess our (relatively small) numerical error.

2. Extrapolation, resolution, and duration tests

Using the ψ_4 extracted on each of the constant-simulation-radius spheres listed above, we have calculated preferred directions and corotating-frame waveforms, both on constant radial slices and using ψ_4 extrapolated to infinity. The preferred direction agrees almost exactly between these different options. Though the simulation-frame and corotating-frame ψ_4 do change

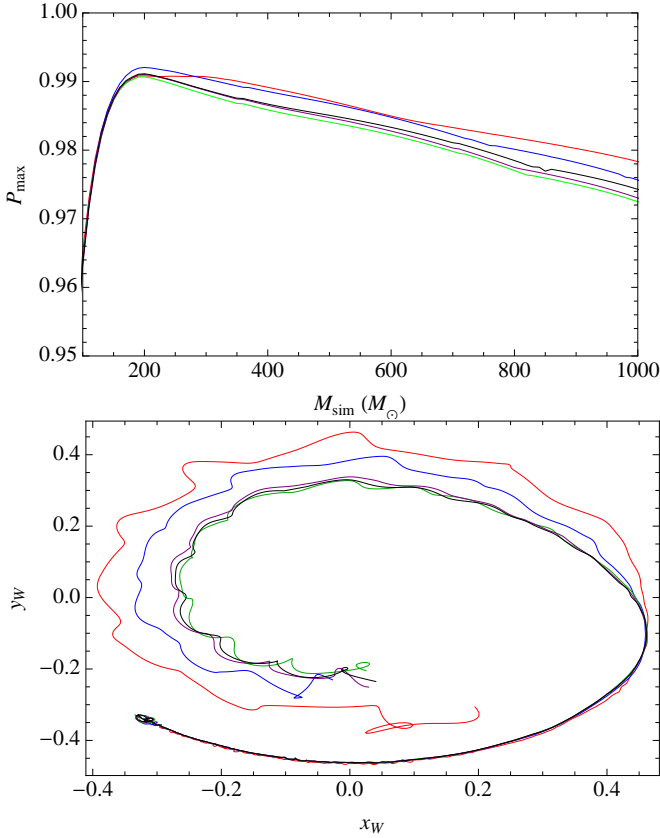


FIG. 11: **Comparing resolutions:** *Top panel:* A plot of $P_{\max, \text{corot}}$ versus mass for the $Sq(4,0.6,270,9)$ simulation, performed at resolutions $h = M/100$ (red), $M/120$ (blue); $M/140$ (green); $M/160$ (purple); and $M/180$ (black). Though significant, the differences between resolutions are nonetheless smaller than the typical differences between simulations; compare to Figure 1. *Bottom panel:* The path of the preferred direction derived from simulations with different resolution, viewed in projection in a frame aligned with the precession cone (i.e., with $\hat{W} \simeq \hat{J}$; see [14]).

slightly with extraction radius, they evolve principally in amplitude and in common. To use a specific quantitative measure that is directly relevant to our principal result, we both evaluated normalized overlaps $\langle \psi_{42,2}(r) | \psi_{42,2}(r') \rangle / |\psi_{42,2}(r)| |\psi_{42,2}(r')|$ between (2,2) modes extracted from different radial slices and evaluated P_{\max} using different extraction radii. For the selected cases examined, the choice of extraction radius had minimal impact ($\Delta P_{\max} \lesssim 0.001$). We therefore limit attention to a single extraction radius ($r = 75M$).

For selected nonprecessing and generic initial configurations, we have also performed simulations at successively higher resolutions. As concrete example, we have performed the $Sq(4,0.6,90,9)$ simulation at resolutions $M/100, M/120, M/140, M/160, M/180$; see Figure 11. Each resolution produces a slightly different duration, with the dominant source of error being a slowly-accumulating phase shift, principally accumulating prior to merger. After recentering our simulations, we find con-

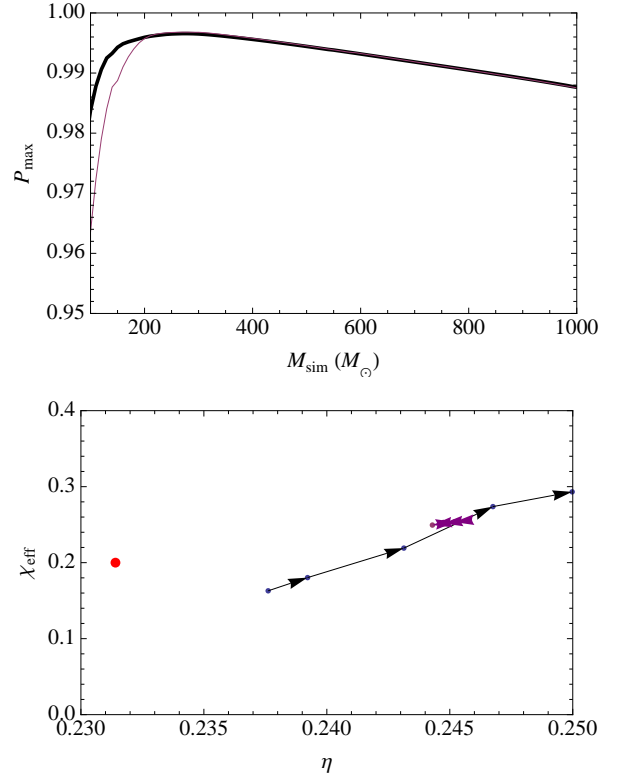


FIG. 12: **Signal duration and the low-mass error:** *Top panel:* The best-fitting match $P_{\max, \text{sim}}$ between IMRPhenomB and the (2,2) mode of an unequal-mass aligned-spin binary [Tq(1.75,0.2,0,10)]. Dotted curve shows P_{\max} derived using the whole signal; solid curve shows P_{\max} derived after first truncating the signal, to mimic the results of a shorter simulation starting at $d = 6.2$. Comparing with Figure 1 and the text, this illustration shows that signal duration dominates our error at low mass and has little impact on our results at high mass. *Bottom panel:* At $M = 100 M_{\odot}$ (blue and black arrows) and $M = 250 M_{\odot}$ (purple arrows), the best-fitting IMRPhenomB parameters which reproduce Tq(1.75,0.2,0,10), truncated to different lengths. For comparison, the red point indicates the corresponding physical properties expected from the initial data. Arrows connect longer to shorter signals, indicating the effect of truncating the signal: a significant error in η and a moderate bias in χ . As illustrated by the discrepancy between the best-fit points and physical parameters, differences between IMRPhenomB model and our simulations also contribute significantly to systematic error in parameter recovery, particularly in mass ratio.

vergence consistent with our differencing order, for the waveform epochs most significant for our results. Our default resolutions (e.g., $M/140$) provide more than enough precision for our most striking results: the persistent precession of \hat{V} long after merger. The lower resolutions used on some shorter simulations are also more than adequate to identify principal features during merger.

Many of our simulations commence shortly prior to merger, from separations as short as $d \simeq 6.2M$. These short (few hundred M) simulations cannot produce a gravitational wave signal from an inspiral which they do

not simulate. To quantify the systematic errors introduced by our choice of signal duration, we have artificially truncated a long, high-resolution nonprecessing signal to a duration comparable to a typical short signal length from $d \simeq 6.2M$. As illustrated in the top panel of Figure 12, this truncated signal matches IMRPhenomB significantly less well than our simulation below $M \simeq 500M_\odot$ but agrees at higher masses. Since signal duration depends sensitively on spin orientation, we believe that most disagreement shown in Figure 1 between our simulations’ corotating-frame signals and IMRPhenomB is dominated by our limited signal duration. In other words, we anticipate the IMRPhenomB model is an adequate representation of any observationally-accessible interval of the corotating-frame signal.

The signal duration of our shortest simulations also imposed a severe limit on our ability to reconstruct the pre-merger binary’s properties using the best-fitting low-mass parameters. As a concrete example, the bottom panel of Figure 12 compares the physical simulation properties (red point) with the parameters derived by fitting IMRPhenomB to a truncated copy of a long, aligned-spin simulation, using $M = 100M_\odot$. Due to systematic differences between IMRPhenomB and our signal, the best-fitting and simulation parameters are significantly offset.

The recovered mass ratio η at low mass depends sensitively on the simulation duration – for the case illustrated here, the best-fit mass ratio changed from $q \simeq 1.5$ to $q \simeq 1$. By contrast, not only was the recovered spin nearly independent of the simulation duration, but also it could be reliably estimated using a much later phase of the signal (i.e., with a much higher mass); see, for example, the purple arrows in Figure 12 and the best-fit spin versus mass shown in Figure 2. For this reason, in the text we use the recovered spin at $M = 300M_\odot$ to illustrate reasonable agreement between the IMRPhenomB model and typical simulations. Using this choice, we could include many more simulations in Figure 9.

Acknowledgments

The authors have benefited from conversations with Andrew Lundgren, Pablo Laguna, William East, Frans Pretorius, and the attendees of the KITP “Chirps, bursts, and mergers” conference. DS is supported by NSF awards PHY-0955825, PHY-1212433 and TG-PHY060013N. ROS is supported by NSF award PHY-0970074 and the UWM Research Growth Initiative.

-
- [1] Abbott et al. (The LIGO Scientific Collaboration), Nuclear Instruments and Methods in Physics Research A **517**, 154 (2004), URL <http://xxx.lanl.gov/abs/gr-qc/0308043>.
 - [2] F. Acernese, P. Amico, M. Alshourbagy, F. Antonucci, S. Aoudia, S. Avino, D. Babusci, G. Ballardin, F. Barone, L. Barsotti, et al., Classical and Quantum Gravity **23**, S635 (2006).
 - [3] M. Punturo et al, Classical and Quantum Gravity **27**, 194002 (2010).
 - [4] T. Prince, in *astro 2010: The Astronomy and Astrophysics Decadal Survey* (2009), pp. 238–+.
 - [5] P. Amaro-Seoane, S. Aoudia, S. Babak, P. Binetruy, E. Berti, A. Bohe, C. Caprini, M. Colpi, N. J. Cornish, K. Danzmann, et al., (arXiv:1202.0839) (2012), URL <http://xxx.lanl.gov/abs/arXiv:1202.0839>.
 - [6] J. Centrella, J. G. Baker, B. J. Kelly, and J. R. van Meter, Reviews of Modern Physics **82**, 3069 (2010).
 - [7] S. T. McWilliams, Classical and Quantum Gravity **28**, 134001 (2011), URL <http://xxx.lanl.gov/abs/arXiv:1012.2872>.
 - [8] A. Taracchini, Y. Pan, A. Buonanno, E. Barausse, M. Boyle, T. Chu, G. Lovelace, H. P. Pfeiffer, and M. A. Scheel, eprint arXiv:1202.0790 (2012), 1202.0790.
 - [9] P. Ajith, M. Boyle, D. A. Brown, B. Brügmann, L. T. Buchman, L. Cadonati, M. Campanelli, T. Chu, Z. B. Etienne, S. Fairhurst, et al., eprint arXiv:1201.5319 (2012), 1201.5319.
 - [10] P. Ajith, M. Hannam, S. Husa, Y. Chen, B. Brügmann, N. Dorband, D. Müller, F. Ohme, D. Pollney, C. Reisswig, et al., Physical Review Letters **106**, 241101 (2011), 0909.2867, URL <http://xxx.lanl.gov/abs/arXiv:0909.2867>.
 - [11] C. O. Lousto, M. Campanelli, Y. Zlochower, and H. Nakano, Classical and Quantum Gravity **27**, 114006 (2010).
 - [12] M. Campanelli, C. Lousto, Y. Zlochower, and D. Merritt, ApJL **659**, L5 (2007), arXiv:gr-qc/0701164.
 - [13] C. O. Lousto and Y. Zlochower, Physical Review Letters **107**, 231102 (2011), 1108.2009.
 - [14] R. O’Shaughnessy, L. London, J. Healy, and D. Shoemaker, Phys. Rev. D **87**, 044038 (2013), 1209.3712.
 - [15] A. Buonanno, L. E. Kidder, A. H. Mroué, H. P. Pfeiffer, and A. Taracchini, Phys. Rev. D **83**, 104034 (2011), URL <http://link.aps.org/doi/10.1103/PhysRevD.83.104034>.
 - [16] R. Sturani et al. (2010), 1005.0551.
 - [17] M. Campanelli, C. O. Lousto, H. Nakano, and Y. Zlochower, Phys. Rev. D **79**, 084010 (2009), 0808.0713.
 - [18] P. Schmidt, M. Hannam, S. Husa, and P. Ajith, Phys. Rev. D **84**, 024046 (2011), URL <http://xxx.lanl.gov/abs/arXiv:1012.2879>.
 - [19] R. O’Shaughnessy, B. Vaishnav, J. Healy, Z. Meeks, and D. Shoemaker, Phys. Rev. D **84**, 124002 (2011), URL <http://link.aps.org/doi/10.1103/PhysRevD.84.124002>.
 - [20] M. Boyle, R. Owen, and H. P. Pfeiffer, Phys. Rev. D **84**, 124011 (2011).
 - [21] P. Schmidt, M. Hannam, and S. Husa, Phys. Rev. D **86**, 104063 (2012), 1207.3088, URL <http://xxx.lanl.gov/abs/arXiv:1207.3088>.
 - [22] C. M. Will and A. G. Wiseman, Phys. Rev. D **54**, 4813 (1996).
 - [23] K. G. Arun, A. Buonanno, G. Faye, and E. Ochsner,

- Phys. Rev. D **79**, 104023 (2009).
- [24] D. Brown, A. Lundgren, and R. O’Shaughnessy, Submitted to PRD (arXiv:1203.6060) (2012), URL <http://arxiv.org/abs/1203.6060>.
 - [25] L. Pekowsky, J. Healy, D. Shoemaker, and P. Laguna, ArXiv e-prints (2012), 1210.1891.
 - [26] R. O’Shaughnessy, J. Healy, L. London, Z. Meeks, and D. Shoemaker, PRD in press (arXiv:1201.2113) (2012), URL <http://xxx.lanl.gov/abs/1201.2113>.
 - [27] H.-S. Cho, E. Ochsner, R. O’Shaughnessy, C. Kim, and C.-H. Lee, Phys. Rev. D **87**, 024004 (2013), 1209.4494.
 - [28] LIGO Scientific Collaboration (2010), URL <https://dcc.ligo.org/cgi-bin/DocDB/ShowDocument?docid=2974>.
 - [29] R. Storn and K. Price, Journal of Global Optimization **11**, 341 (1997), ISSN 0925-5001, URL <http://dx.doi.org/10.1023/A%3A1008202821328>.
 - [30] E. Poisson and C. M. Will, Phys. Rev. D **52**, 848 (1995), arXiv:gr-qc/9502040.
 - [31] T. Damour, Phys. Rev. D **64**, 124013 (2001), arXiv:gr-qc/0103018.
 - [32] P. Ajith, Phys. Rev. D **84**, 084037 (2011), 1107.1267.
 - [33] L. Santamaria, F. Ohme, P. Ajith, B. Bruegmann, N. Dorband, M. Hannam, S. Husa, P. Moesta, D. Pollney, C. Reisswig, et al., (arXiv:1005.3306) (2010), URL <http://xxx.lanl.gov/abs/arXiv:1005.3306>.
 - [34] C. Cutler and E. E. Flanagan, Phys. Rev. D **49**, 2658 (1994), gr-qc/9402014.
 - [35] C. O. Lousto, H. Nakano, Y. Zlochower, and M. Campanelli, Phys. Rev. D **81**, 084023 (2010), 0910.3197.
 - [36] L. Boyle, M. Kesden, and S. Nissanke, Physical Review Letters **100**, 151101 (2008), 0709.0299, URL <http://xxx.lanl.gov/abs/arXiv:0709.0299>.
 - [37] L. Boyle and M. Kesden, Phys. Rev. D **78**, 024017 (2008), 0712.2819.
 - [38] L. Rezzolla, Classical and Quantum Gravity **26**, 094023 (2009), 0812.2325.
 - [39] E. Barausse, V. Morozova, and L. Rezzolla, Astrophys. J. **758**, 63 (2012), 1206.3803, URL <http://xxx.lanl.gov/abs/arXiv:1206.3803>.
 - [40] M. Kesden, U. Sperhake, and E. Berti, Phys. Rev. D **81**, 084054 (2010), 1002.2643.
 - [41] M. Kesden, U. Sperhake, and E. Berti, Astrophys. J. **715**, 1006 (2010), 1003.4993.
 - [42] E. Barausse and L. Rezzolla, ApJL **704**, L40 (2009), 0904.2577.
 - [43] T. A. Apostolatos, C. Cutler, G. J. Sussman, and K. S. Thorne, Phys. Rev. D **49**, 6274 (1994).
 - [44] E. Ochsner and R. O’Shaughnessy, in LSC review (DCC P120043); to be submitted to PRD (2012).
 - [45] P. Ajith and S. Bose, Phys. Rev. D **79**, 084032 (2009), 0901.4936.
 - [46] Abadie et al (LIGO Scientific Collaboration), Nuclear Instruments and Methods in Physics Research Section A: Accelerators, Spectrometers, Detectors and Associated Equipment **624**, 223 (2010), ISSN 0168-9002, URL <http://www.sciencedirect.com/science/article/pii/S0168900210017031>.
 - [47] J. G. Baker, W. D. Boggs, J. Centrella, B. J. Kelly, S. T. McWilliams, and J. R. van Meter, Phys. Rev. D **78**, 044046 (2008), 0805.1428.
 - [48] K. S. Thorne, Reviews of Modern Physics **52**, 299 (1980).
 - [49] J. D. Schnittman, A. Buonanno, J. R. van Meter, J. G. Baker, W. D. Boggs, J. Centrella, B. J. Kelly, and S. T. McWilliams, Phys. Rev. D **77**, 044031 (2008), 0707.0301.
 - [50] F. Herrmann, I. Hinder, D. Shoemaker, and P. Laguna, Classical and Quantum Gravity **24**, S33 (2007), arXiv:gr-qc/0601026.
 - [51] F. Herrmann, I. Hinder, D. M. Shoemaker, P. Laguna, and R. A. Matzner, Phys. Rev. **D76**, 084032 (2007), 0706.2541.
 - [52] F. Herrmann, I. Hinder, D. Shoemaker, P. Laguna, and R. A. Matzner, Astrophys. J. **661**, 430 (2007), gr-qc/0701143.
 - [53] I. Hinder, B. Vaishnav, F. Herrmann, D. Shoemaker, and P. Laguna, Phys. Rev. **D77**, 081502 (2008), 0710.5167.
 - [54] J. Healy et al., Phys. Rev. Lett. **102**, 041101 (2009), 0807.3292.
 - [55] I. Hinder, F. Herrmann, P. Laguna, and D. Shoemaker, **arxiv:0806.1037** (2008), 0806.1037.
 - [56] J. Healy, J. Levin, and D. Shoemaker, Phys. Rev. Lett. **103**, 131101 (2009), 0907.0671.
 - [57] J. Healy, P. Laguna, R. A. Matzner, and D. M. Shoemaker, Phys. Rev. **D81**, 081501 (2010), 0905.3914.
 - [58] T. Bode, R. Haas, T. Bogdanovic, P. Laguna, and D. Shoemaker, Astrophys. J. **715**, 1117 (2010), 0912.0087.
 - [59] E. Schnetter, S. H. Hawley, and I. Hawke, Class. Quant. Grav. **21**, 1465 (2004).
 - [60] cactus-web, cactus Computational Toolkit home page: <http://www.cactuscode.org>.
 - [61] S. Husa, I. Hinder, and C. Lechner, Computer Physics Communications **174**, 983 (2006).
 - [62] R. O’Shaughnessy, B. Vaishnav, J. Healy, and D. Shoemaker, Phys. Rev. D **82**, 104006 (2010), URL <http://xxx.lanl.gov/abs/arXiv:1007.4213>.
-

TABLE I: **Simulations:** The first column is a key, encoding the family, mass ratio, black hole spin magnitude(s) $|S_1|/M_1^2$ and $|S_2|/M_2^2$ and alignment. The next column is the simulation resolution h/M . In a handful of cases used as resolution tests in the text, multiple resolutions of the same initial data appear in the table. The next 8 columns provide specific initial conditions: the initial separation (r_{start}), mass ratio $q = m_1/m_2$, and two component spins S_k^2/M^2 relative to the total initial mass. The column labelled T_{wave} provides an estimate of the duration of the well-resolved ψ_{422} mode. The column labelled χ_{PB} evaluates χ_{PB} [Eq. (9)] using the specific mass ratio and spins provided in previous columns. Finally, the last two columns provide the final black hole mass and angular momentum, derived from the late-time horizon.

Key	h^{-1} M^{-1}	r_{start} M	q	$S_{1,x}$ M^2	$S_{1,y}$ M^2	$S_{1,z}$ M^2	$S_{2,x}$ M^2	$S_{2,y}$ M^2	$S_{2,z}$ M^2	T_{wave} M	$\chi_{PB,sim}$	M_f M	J_f M_f^2
Eq(2.5, 0.6, 0, 7)	140	7	2.5	0.3061	0	0	-0.049	0	0	310.	0	0.965	0.632
Eq(2.5, 0.6, 30, 7)	140	7	2.5	0.2651	0.153	0	-0.0424	-0.0245	0	310.	0	0.965	0.632
Eq(2.5, 0.6, 60, 7)	140	7	2.5	0.153	0.2651	0	-0.0245	-0.0424	0	310.	0	0.966	0.636
Eq(2.5, 0.6, 90, 7)	140	7	2.5	0	0.3061	0	0	-0.049	0	310.	0	0.966	0.637
Eq(2.5, 0.6, 120, 7)	140	7	2.5	-0.153	0.2651	0	0.0245	-0.0424	0	320.	0	0.966	0.636
Eq(2.5, 0.6, 150, 7)	140	7	2.5	-0.2651	0.153	0	0.0424	-0.0245	0	320.	0	0.965	0.634
Eq(2.5, 0.6, 180, 7)	140	7	2.5	-0.3061	0	0	0.049	0	0	320.	0	0.965	0.632
Eq(2.5, 0.6, 210, 7)	140	7	2.5	-0.2651	-0.153	0	0.0424	0.0245	0	320.	0	0.965	0.632
Eq(2.5, 0.6, 240, 7)	140	7	2.5	-0.153	-0.2651	0	0.0245	0.0424	0	310.	0	0.966	0.636
Eq(2.5, 0.6, 270, 7)	140	7	2.5	0	-0.3061	0	0	0.049	0	310.	0	0.966	0.637
Eq(2.5, 0.6, 300, 7)	140	7	2.5	0.153	-0.2651	0	-0.0245	0.0424	0	310.	0	0.966	0.636
Eq(2.5, 0.6, 330, 7)	140	7	2.5	0.2651	-0.153	0	-0.0424	0.0245	0	310.	0	0.965	0.634
Eq(3., 0.6, 0, 7)	140	7	3.	0.3375	0	0	-0.0375	0	0	320.	0	0.97	0.619
Eq(3., 0.6, 30, 7)	140	7	3.	0.2923	0.1687	0	-0.0325	-0.0187	0	320.	0	0.969	0.616
Eq(3., 0.6, 60, 7)	140	7	3.	0.1687	0.2923	0	-0.0187	-0.0325	0	310.	0	0.969	0.616
Eq(3., 0.6, 90, 7)	140	7	3.	0	0.3375	0	0	-0.0375	0	310.	0	0.97	0.619
Eq(3., 0.6, 120, 7)	140	7	3.	-0.1687	0.2923	0	0.0187	-0.0325	0	320.	0	0.97	0.62
Eq(3., 0.6, 150, 7)	140	7	3.	-0.2923	0.1687	0	0.0325	-0.0187	0	320.	0	0.97	0.62
Eq(3., 0.6, 180, 7)	140	7	3.	-0.3375	0	0	0.0375	0	0	330.	0	0.97	0.619
Eq(3., 0.6, 210, 7)	140	7	3.	-0.2923	-0.1687	0	0.0325	0.0187	0	330.	0	0.969	0.616
Eq(3., 0.6, 240, 7)	140	7	3.	-0.1687	-0.2923	0	0.0187	0.0325	0	320.	0	0.969	0.616
Eq(3., 0.6, 270, 7)	140	7	3.	0	-0.3375	0	0	0.0375	0	320.	0	0.97	0.619
Eq(3., 0.6, 300, 7)	140	7	3.	0.1687	-0.2923	0	-0.0187	0.0325	0	320.	0	0.97	0.62
Eq(3., 0.6, 330, 7)	140	7	3.	0.2923	-0.1687	0	-0.0325	0.0187	0	320.	0	0.97	0.62
Lq(2.5, 0.6, 0, 6.2)	140	6.2	2.5	0	0	0.3061	0	0	0.049	410.	0.6	0.947	0.825
Lq(2.5, 0.6, 15, 6.2)	140	6.2	2.5	0.0792	0	0.2957	-0.0127	0	0.0473	390.	0.58	0.948	0.82
Lq(2.5, 0.6, 30, 6.2)	140	6.2	2.5	0.153	0	0.2651	-0.0245	0	0.0424	370.	0.52	0.951	0.804
Lq(2.5, 0.6, 45, 6.2)	140	6.2	2.5	0.2164	0	0.2164	-0.0346	0	0.0346	350.	0.42	0.953	0.775
Lq(2.5, 0.6, 60, 6.2)	140	6.2	2.5	0.2651	0	0.153	-0.0424	0	0.0245	310.	0.3	0.957	0.737
Lq(2.5, 0.6, 75, 6.2)	140	6.2	2.5	0.2957	0	0.0792	-0.0473	0	0.0127	280.	0.16	0.962	0.693
Lq(2.5, 0.6, 90, 6.2)	140	6.2	2.5	0.3061	0	0	-0.0489	0	0	250.	0	0.965	0.631
Lq(2.5, 0.6, 120, 6.2)	140	6.2	2.5	0.2651	0	-0.153	-0.0424	0	-0.0245	190.	-0.3	0.971	0.499
Lq(2.5, 0.6, 150, 6.2)	140	6.2	2.5	0.153	0	-0.2651	-0.0245	0	-0.0424	170.	-0.52	0.975	0.373
Lq(2.5, 0.6, 210, 6.2)	140	6.2	2.5	-0.153	0	-0.2651	0.0245	0	-0.0424	170.	-0.52	0.975	0.373
Lq(2.5, 0.6, 240, 6.2)	140	6.2	2.5	-0.2651	0	-0.153	0.0424	0	-0.0245	200.	-0.3	0.971	0.499
Lq(2.5, 0.6, 270, 6.2)	140	6.2	2.5	-0.3061	0	0	0.0489	0	0	240.	0	0.965	0.631
Lq(2.5, 0.6, 300, 6.2)	140	6.2	2.5	-0.2651	0	0.153	0.0424	0	0.0245	320.	0.3	0.957	0.737
Lq(2.5, 0.6, 315, 6.2)	140	6.2	2.5	-0.2164	0	0.2164	0.0346	0	0.0346	350.	0.42	0.954	0.775
Lq(2.5, 0.6, 330, 6.2)	140	6.2	2.5	-0.153	0	0.2651	0.0245	0	0.0424	370.	0.52	0.951	0.804
Lq(2.5, 0.6, 345, 6.2)	140	6.2	2.5	-0.0792	0	0.2957	0.0127	0	0.0473	400.	0.58	0.948	0.82
Lq(3., 0.6, 30, 6.2)	140	6.2	3.	0.1687	0	0.2923	-0.0187	0	0.0325	390.	0.52	0.957	0.791
Lq(3., 0.6, 45, 6.2)	140	6.2	3.	0.2386	0	0.2386	-0.0265	0	0.0265	360.	0.42	0.959	0.763
Lq(3., 0.6, 60, 6.2)	140	6.2	3.	0.2923	0	0.1687	-0.0325	0	0.0187	330.	0.3	0.963	0.727
Lq(3., 0.6, 210, 6.2)	140	6.2	3.	-0.1687	0	-0.2922	0.0187	0	-0.0324	160.	-0.52	0.978	0.324
Lq(3., 0.6, 240, 6.2)	140	6.2	3.	-0.2923	0	-0.1687	0.0325	0	-0.0187	200.	-0.3	0.975	0.472
Lq(3., 0.6, 270, 6.2)	140	6.2	3.	-0.3375	0	0	0.0375	0	0	240.	0	0.969	0.615
S(1, 0.2, 0)	77	6.2	1	0	0	0.05	-0.05	0	0	250.	0.10	0.95	0.802
S(1, 0.2, 45)	77	6.2	1	0.0354	0	0.0354	-0.05	0	0	250.	0.071	0.951	0.788
S(1, 0.2, 90)	77	6.2	1	0.05	0	0	-0.05	0	0	220.	0	0.953	0.76

S(1, 0.2, 135)	77	6.2	1	0.0354	0	-0.0354	-0.05	0	0	210.	-0.071	0.954	0.734
S(1, 0.2, 180)	77	6.2	1	0	0	-0.05	-0.05	0	0	210.	-0.10	0.955	0.725
S(1, 0.2, 225)	77	6.2	1	-0.0354	0	-0.0354	-0.05	0	0	210.	-0.071	0.954	0.743
S(1, 0.2, 270)	77	6.2	1	-0.05	0	0	-0.05	0	0	220.	0	0.952	0.774
S(1, 0.2, 315)	77	6.2	1	-0.0354	0	0.0354	-0.05	0	0	250.	0.071	0.951	0.798
S(1, 0.4, 0)	77	6.2	1	0	0	0.1	-0.1	0	0	280.	0.20	0.946	0.849
S(1, 0.4, 45)	77	6.2	1	0.0707	0	0.0707	-0.1	0	0	260.	0.14	0.948	0.814
S(1, 0.4, 90)	77	6.2	1	0.1	0	0	-0.1	0	0	230.	0	0.953	0.76
S(1, 0.4, 135)	77	6.2	1	0.0707	0	-0.0707	-0.1	0	0	210.	-0.14	0.956	0.706
S(1, 0.4, 180)	77	6.2	1	0	0	-0.1	-0.1	0	0	210.	-0.20	0.957	0.697
S(1, 0.4, 225)	77	6.2	1	-0.0707	0	-0.0707	-0.1	0	0	210.	-0.14	0.955	0.744
S(1, 0.4, 270)	77	6.2	1	-0.1	0	0	-0.1	0	0	240.	0	0.952	0.813
S(1, 0.4, 315)	77	6.2	1	-0.0707	0	0.0707	-0.1	0	0	270.	0.14	0.948	0.853
S(1, 0.6, 0)	77	6.2	1	0	0	0.15	-0.15	0	0	290.	0.30	0.942	0.904
S(1, 0.6, 15)	77	6.2	1	0.0388	0	0.1449	-0.15	0	0	290.	0.29	0.943	0.887
S(1, 0.6, 30)	77	6.2	1	0.075	0	0.1299	-0.15	0	0	280.	0.26	0.944	0.866
S(1, 0.6, 45)	77	6.2	1	0.1061	0	0.1061	-0.15	0	0	270.	0.21	0.945	0.841
S(1, 0.6, 60)	77	6.2	1	0.1299	0	0.075	-0.15	0	0	260.	0.15	0.946	0.814
S(1, 0.6, 75)	77	6.2	1	0.1449	0	0.0388	-0.15	0	0	250.	0.078	0.949	0.788
S(1, 0.6, 90)	77	6.2	1	0.15	0	0	-0.15	0	0	230.	0	0.953	0.759
S(1, 0.6, 105)	77	6.2	1	0.1449	0	-0.0388	-0.15	0	0	200.	-0.078	0.954	0.728
S(1, 0.6, 120)	77	6.2	1	0.1299	0	-0.075	-0.15	0	0	210.	-0.15	0.955	0.699
S(1, 0.6, 135)	77	6.2	1	0.1061	0	-0.1061	-0.15	0	0	210.	-0.21	0.957	0.679
S(1, 0.6, 150)	77	6.2	1	0.075	0	-0.1299	-0.15	0	0	200.	-0.26	0.958	0.667
S(1, 0.6, 165)	77	6.2	1	0.0388	0	-0.1449	-0.15	0	0	200.	-0.29	0.959	0.665
S(1, 0.6, 180)	77	6.2	1	0	0	-0.15	-0.15	0	0	200.	-0.30	0.959	0.675
S(1, 0.6, 195)	77	6.2	1	-0.0388	0	-0.1449	-0.15	0	0	200.	-0.29	0.959	0.696
S(1, 0.6, 210)	77	6.2	1	-0.075	0	-0.1299	-0.15	0	0	200.	-0.26	0.957	0.726
S(1, 0.6, 225)	77	6.2	1	-0.1061	0	-0.1061	-0.15	0	0	210.	-0.21	0.955	0.761
S(1, 0.6, 240)	77	6.2	1	-0.1299	0	-0.075	-0.15	0	0	200.	-0.15	0.954	0.8
S(1, 0.6, 255)	77	6.2	1	-0.1449	0	-0.0388	-0.15	0	0	230.	-0.078	0.953	0.839
S(1, 0.6, 260)	77	6.2	1	-0.1477	0	-0.026	-0.15	0	0	250.	-0.052	0.953	0.851
S(1, 0.6, 265)	77	6.2	1	-0.1494	0	-0.0131	-0.15	0	0	250.	-0.026	0.952	0.862
S(1, 0.6, 270)	77	6.2	1	-0.15	0	0	-0.15	0	0	250.	0	0.951	0.873
S(1, 0.6, 285)	77	6.2	1	-0.1449	0	0.0388	-0.15	0	0	270.	0.078	0.948	0.899
S(1, 0.6, 300)	77	6.2	1	-0.1299	0	0.075	-0.15	0	0	280.	0.15	0.945	0.917
S(1, 0.6, 315)	77	6.2	1	-0.1061	0	0.1061	-0.15	0	0	290.	0.21	0.943	0.925
S(1, 0.6, 330)	77	6.2	1	-0.075	0	0.1299	-0.15	0	0	290.	0.26	0.943	0.925
S(1, 0.6, 345)	77	6.2	1	-0.0388	0	0.1449	-0.15	0	0	290.	0.29	0.942	0.917
S(1, 0.8, 0)	77	6.2	1	0	0	0.2	-0.2	0	0	310.	0.40	0.938	0.936
S(1, 0.8, 120)	77	6.2	1	0.1732	0	-0.1	-0.2	0	0	210.	-0.20	0.955	0.676
S(1, 0.8, 150)	77	6.2	1	0.1	0	-0.1732	-0.2	0	0	200.	-0.35	0.96	0.634
S(1, 0.8, 180)	77	6.2	1	0	0	-0.2	-0.2	0	0	190.	-0.40	0.961	0.641
S(1, 0.8, 210)	77	6.2	1	-0.1	0	-0.1732	-0.2	0	0	200.	-0.35	0.958	0.698
S(1, 0.8, 240)	77	6.2	1	-0.1732	0	-0.1	-0.2	0	0	230.	-0.2	0.954	0.783
S(1, 0.8, 255)	77	6.2	1	-0.1932	0	-0.0518	-0.2	0	0	260.	-0.10	0.954	0.83
S(1, 0.8, 270)	77	6.2	1	-0.2	0	0	-0.2	0	0	280.	0	0.947	0.866
S(1, 0.8, 30)	77	6.2	1	0.1	0	0.1732	-0.2	0	0	290.	0.35	0.94	0.898
S(1, 0.8, 300)	77	6.2	1	-0.1732	0	0.1	-0.2	0	0	290.	0.20	0.943	0.923
S(1, 0.8, 330)	77	6.2	1	-0.1	0	0.1732	-0.2	0	0	310.	0.35	0.94	0.948
S(1, 0.8, 60)	77	6.2	1	0.1732	0	0.1	-0.2	0	0	270.	0.20	0.944	0.83
S(1, 0.8, 90)	77	6.2	1	0.2	0	0	-0.2	0	0	230.	0.	0.952	0.758
S(1, 0.6, 0, 8)	77	8	1	0	0	0.15	-0.15	0	0		0.30		
S(1, 0.6, 135, 8)	77	8	1	0.1061	0	-0.1061	-0.15	0	0		-0.21		
S(1, 0.6, 180, 8)	77	8	1	0	0	-0.15	-0.15	0	0		-0.30		
S(1, 0.6, 225, 8)	77	8	1	-0.1061	0	-0.1061	-0.15	0	0		-0.21		
S(1, 0.6, 240, 8)	77	8	1	-0.1299	0	-0.075	-0.15	0	0		-0.15		
S(1, 0.6, 255, 8)	77	8	1	-0.1449	0	-0.0388	-0.15	0	0		-0.078		
S(1, 0.6, 270, 8)	77	8	1	-0.15	0	0	-0.15	0	0		0		
S(1, 0.6, 315, 8)	77	8	1	-0.1061	0	0.1061	-0.15	0	0		0.21		
S(1, 0.6, 45, 8)	77	8	1	0.1061	0	0.1061	-0.15	0	0		0.21		
S(1, 0.6, 90, 8)	77	8	1	0.15	0	0	-0.15	0	0		0		
Sq(2, 0.6, 0, 6.2)	120	6.2	2	0	0	0.2666	-0.0666	0	0	340.	0.40	0.946	0.81
Sq(2, 0.6, 150, 6.2)	120	6.2	2	0.1333	0	-0.2309	-0.0666	0	0	200.	-0.35	0.969	0.457

Sq(2, 0.6, 180, 6.2)	120	6.2	2	0	0	-0.2666	-0.0666	0	0	190.	-0.40	0.97	0.429
Sq(2, 0.6, 90, 6.2)	120	6.2	2	0.2666	0	0	-0.0666	0	0	260.	0	0.96	0.652
Sq(2.5, 0.6, 0, 6.2)	120	6.2	2.5	0	0	0.3061	-0.0489	0	0	370.	0.43	0.952	0.805
Sq(2.5, 0.6, 120, 6.2)	120	6.2	2.5	0.2651	0	-0.153	-0.0489	0	0	210.	-0.21	0.97	0.51
Sq(2.5, 0.6, 15, 6.2)	120	6.2	2.5	0.0792	0	0.2957	-0.0489	0	0	360.	0.41	0.952	0.797
Sq(2.5, 0.6, 150, 6.2)	120	6.2	2.5	0.153	0	-0.2651	-0.0489	0	0	180.	-0.37	0.974	0.389
Sq(2.5, 0.6, 180, 6.2)	120	6.2	2.5	0	0	-0.3061	-0.0489	0	0	180.	-0.43	0.975	0.344
Sq(2.5, 0.6, 210, 6.2)	120	6.2	2.5	-0.153	0	-0.2651	-0.0489	0	0	190.	-0.37	0.973	0.421
Sq(2.5, 0.6, 240, 6.2)	120	6.2	2.5	-0.2651	0	-0.153	-0.0489	0	0	230.	-0.21	0.97	0.552
Sq(2.5, 0.6, 270, 6.2)	120	6.2	2.5	-0.3061	0	0	-0.0489	0	0	270.	0	0.964	0.668
Sq(2.5, 0.6, 30, 6.2)	120	6.2	2.5	0.153	0	0.2651	-0.0489	0	0	350.	0.37	0.954	0.783
Sq(2.5, 0.6, 300, 6.2)	120	6.2	2.5	-0.2651	0	0.153	-0.0489	0	0	330.	0.21	0.958	0.75
Sq(2.5, 0.6, 315, 6.2)	120	6.2	2.5	-0.2164	0	0.2164	-0.0489	0	0	340.	0.3	0.955	0.776
Sq(2.5, 0.6, 330, 6.2)	120	6.2	2.5	-0.153	0	0.2651	-0.0489	0	0	360.	0.37	0.953	0.795
Sq(2.5, 0.6, 345, 6.2)	120	6.2	2.5	-0.0792	0	0.2957	-0.0489	0	0	370.	0.41	0.952	0.804
Sq(2.5, 0.6, 45, 6.2)	120	6.2	2.5	0.2164	0	0.2164	-0.0489	0	0	330.	0.3	0.957	0.759
Sq(2.5, 0.6, 60, 6.2)	120	6.2	2.5	0.2651	0	0.153	-0.0489	0	0	300.	0.21	0.958	0.724
Sq(2.5, 0.6, 75, 6.2)	120	6.2	2.5	0.2957	0	0.0792	-0.0489	0	0	280.	0.11	0.963	0.686
Sq(2.5, 0.6, 90, 6.2)	120	6.2	2.5	0.3061	0	0	-0.0489	0	0	260.	0	0.965	0.631
Sq(3, 0.6, 0, 6.2)	120	6.2	3	0	0	0.3375	-0.0375	0	0	390.	0.45	0.957	0.798
Sq(3, 0.6, 120, 6.2)	120	6.2	3	0.2923	0	-0.1687	-0.0375	0	0	210.	-0.22	0.975	0.479
Sq(3, 0.6, 15, 6.2)	120	6.2	3	0.0873	0	0.326	-0.0375	0	0	380.	0.43	0.958	0.791
Sq(3, 0.6, 30, 6.2)	120	6.2	3	0.1687	0	0.2923	-0.0375	0	0	370.	0.39	0.959	0.774
Sq(3, 0.6, 45, 6.2)	120	6.2	3	0.2386	0	0.2386	-0.0375	0	0	350.	0.32	0.962	0.752
Sq(3, 0.6, 60, 6.2)	120	6.2	3	0.2923	0	0.1687	-0.0375	0	0	320.	0.22	0.964	0.715
Sq(3, 0.6, 75, 6.2)	120	6.2	3	0.326	0	0.0873	-0.0375	0	0	290.	0.12	0.967	0.674
Sq(3, 0.6, 90, 6.2)	120	6.2	3	0.3375	0	0	-0.0375	0	0	260.	0	0.969	0.615
Sq(3, 0.6, 150, 6.2)	120	6.2	3	0.1687	0	-0.2922	-0.0375	0	0	170.	-0.39	0.978	0.333
Sq(3, 0.6, 180, 6.2)	120	6.2	3	0	0	-0.3374	-0.0375	0	0	180.	-0.45	0.978	0.269
Sq(3, 0.6, 210, 6.2)	120	6.2	3	-0.1687	0	-0.2922	-0.0375	0	0	180.	-0.39	0.977	0.364
Sq(3, 0.6, 240, 6.2)	120	6.2	3	-0.2923	0	-0.1687	-0.0375	0	0	220.	-0.22	0.974	0.517
Sq(3, 0.6, 270, 6.2)	120	6.2	3	-0.3375	0	0	-0.0375	0	0	270.	0	0.969	0.648
Sq(3, 0.6, 300, 6.2)	120	6.2	3	-0.2923	0	0.1687	-0.0375	0	0	340.	0.22	0.963	0.736
Sq(3, 0.6, 315, 6.2)	120	6.2	3	-0.2386	0	0.2386	-0.0375	0	0	360.	0.32	0.96	0.765
Sq(3, 0.6, 330, 6.2)	120	6.2	3	-0.1687	0	0.2923	-0.0375	0	0	380.	0.39	0.959	0.786
Sq(3, 0.6, 345, 6.2)	120	6.2	3	-0.0873	0	0.326	-0.0375	0	0	390.	0.43	0.957	0.796
Sq(4, 0.6, 0, 6.2)	120	6.2	4	0	0	0.384	-0.024	0	0	430.	0.48	0.966	0.781
Sq(4, 0.6, 0, 9, 6.2)	120	9	4	0	0	0.384	-0.024	0	0	1300.	0.48	0.965	0.779
Sq(4, 0.6, 30, 6.2)	120	6.2	4	0.192	0	0.3325	-0.024	0	0	430.	0.42	0.967	0.759
Sq(4, 0.6, 90, 6.2)	120	6.2	4	0.384	0	0	-0.024	0	0	260.	0	0.977	0.594
Sq(4, 0.6, 90, 9)	120	9	4	0.384	0	0	-0.024	0	0	870.	0	0.976	0.593
Sq(4, 0.6, 150, 6.2)	120	6.2	4	0.192	0	-0.3325	-0.024	0	0	170.	-0.42	0.983	0.255
Sq(4, 0.6, 150, 9)	120	9	4	0.192	0	-0.3325	-0.024	0	0	460.	-0.42	0.983	0.258
Sq(4, 0.6, 180, 6.2)	120	6.2	4	0	0	-0.384	-0.024	0	0	170.	-0.48	0.983	0.146
Sq(4, 0.6, 180, 9)	120	9	4	0	0	-0.384	-0.024	0	0	430.	-0.48	0.983	0.15
Sq(4, 0.6, 210, 9)	120	9	4	-0.192	0	-0.3325	-0.024	0	0	490.	-0.42	0.982	0.285
Sq(4, 0.6, 270, 6.2)	120	6.2	4	-0.384	0	0	-0.024	0	0	280.	0	0.976	0.616
Sq(4, 0.6, 270, 9)	120	9	4	-0.384	0	0	-0.024	0	0	890.	0	0.975	0.612
Sq(4, 0.6, 270, 9)	140	9	4	-0.384	0	0	-0.024	0	0	890.	0	0.975	0.612
Sq(4, 0.6, 270, 9)	160	9	4	-0.384	0	0	-0.024	0	0	890.	0	0.975	0.612
Sq(4, 0.6, 270, 9)	180	9	4	-0.384	0	0	-0.024	0	0	890.	0	0.975	0.613
T(1, 0., 0)	77	6.2	1	0	0	0	0	0	0	890.	0	0.951	0.685
T(1, 0.2, 0)	77	6.2	1	0	0	0.05	0	0	0.05	910.	0.2		
T(1, 0.2, 45)	77	6.2	1	0	0	0.05	0.0354	0	0.0354	850.	0.17		
T(1, 0.2, 60)	77	6.2	1	0	0	0.05	0.0433	0	0.025	840.	0.15		
T(1, 0.2, 90)	77	6.2	1	0	0	0.05	0.05	0	0	840.	0.1		
T(1, 0.4, 0)	90	6.2	1	0	0	0.1	0	0	0.1	1000.	0.4		
T(1, 0.4, 45)	77	6.2	1	0	0	0.1	0.0707	0	0.0707	990.	0.34		
T(1, 0.4, 60)	77	6.2	1	0	0	0.1	0.0866	0	0.05	970.	0.3		
T(1, 0.4, 90)	77	6.2	1	0	0	0.1	0.1	0	0	910.	0.2		
T(1, 0.6, 0)	77	6.2	1	0	0	0.15	0	0	0.15	1100.	0.6		
T(1, 0.6, 45)	77	6.2	1	0	0	0.15	0.1061	0	0.1061	1100.	0.51		
T(1, 0.6, 60)	77	6.2	1	0	0	0.15	0.1299	0	0.075	990.	0.45		
T(1, 0.6, 90)	77	6.2	1	0	0	0.15	0.15	0	0	920.	0.3		

T(1, 0.8, 0)	90	6.2	1	0	0	0.2	0	0	0.2	1200.	0.8	0.906	0.9
Tq(1.5, 0.4, 60, 10)	120	10	1.5	0.1247	0	0.072	0	0	0.064	1200.	0.28	0.947	0.753
Tq(1.5, 0.6, 45, 10)	120	10	1.5	0.1527	0	0.1527	0	0	0.096	1300.	0.49	0.937	0.822
Tq(2, 0.4, 60, 10)	120	10	2	0.1539	0	0.0889	0	0	0.0444	1200.	0.27	0.954	0.722
Tq(2, 0.6, 135, 10)	120	10	2	0.1885	0	-0.1885	0	0	0.0666	930.	-0.083	0.964	0.549
Tq(2, 0.6, 180, 10)	120	10	2	0	0	-0.2666	0	0	0.0666	810.	-0.20	0.967	0.465
Tq(2, 0.6, 270, 10)	120	10	2	-0.2666	0	0	0	0	0.0666	1200.	0.20	0.955	0.698
Tq(2, 0.6, 45, 10)	120	10	2	0.1885	0	0.1885	0	0	0.0666	1400.	0.48	0.945	0.804
Tq(2, 0.6, 60, 10)	120	10	2	0.2309	0	0.1333	0	0	0.0666	1300.	0.40	0.948	0.777
Tq(2, 0.6, 90, 10)	120	10	2	0.2666	0	0	0	0	0.0666	1200.	0.20	0.955	0.698
Tq(2.5, 0.4, 45, 10)	120	10	2.5	0.1443	0	0.1443	0	0	0.0326	1400.	0.32	0.958	0.715
Tq(2.5, 0.4, 60, 10)	120	10	2.5	0.1767	0	0.102	0	0	0.0326	1300.	0.26	0.96	0.693
Tq(2.5, 0.4, 90, 10)	120	10	2.5	0.2041	0	0	0	0	0.0326	1200.	0.11	0.964	0.626
Tq(2.5, 0.6, 45, 10)	120	10	2.5	0.2164	0	0.2165	0	0	0.049	1500.	0.47	0.952	0.787
Tq(2.5, 0.6, 60, 10)	120	10	2.5	0.2651	0	0.1531	0	0	0.049	1400.	0.39	0.955	0.756
Tq(2.5, 0.6, 90, 10)	120	10	2.5	0.3061	0	0	0	0	0.049	1200.	0.17	0.962	0.671
Tq(4, 0.6, 45, 10)	120	10	4	0.2715	0	0.2715	0	0	0.024	1800.	0.46	0.968	0.749
Tq(4, 0.6, 60, 10)	120	10	4	0.3325	0	0.192	0	0	0.024	1700.	0.36	0.97	0.715
Tq(4, 0.6, 90, 10)	120	10	4	0.384	0	0	0	0	0.024	1400.	0.12	0.975	0.61
V(1, 0.6, 34, 0)	77	6.2	1	0.0839	0	0.1243	-0.0839	0	0.1243	290.	0.50		
V(1, 0.6, 34, 30)	77	6.2	1	0.0726	0.0419	0.1243	-0.0726	-0.0419	0.1243	290.	0.50		
V(1, 0.6, 34, 45)	77	6.2	1	0.0593	0.0593	0.1243	-0.0593	-0.0593	0.1243	290.	0.50		
V(1, 0.6, 34, 60)	77	6.2	1	0.0419	0.0726	0.1243	-0.0419	-0.0726	0.1243	290.	0.50		
V(1, 0.6, 34, 90)	77	6.2	1	0	0.0839	0.1243	0	-0.0839	0.1243	300.	0.50	0.932	0.827
V(1, 0.6, 34, 120)	77	6.2	1	-0.0419	0.0726	0.1243	0.0419	-0.0726	0.1243	300.	0.50	0.933	0.828
V(1, 0.6, 34, 150)	77	6.2	1	-0.0726	0.0419	0.1243	0.0726	-0.0419	0.1243	300.	0.50	0.933	0.829
V(1, 0.6, 34, 180)	77	6.2	1	-0.0839	0	0.1243	0.0839	0	0.1243	300.	0.50		
V(1, 0.6, 34, 210)	77	6.2	1	-0.0726	-0.0419	0.1243	0.0726	0.0419	0.1243	320.	0.5		
V(1, 0.6, 34, 240)	77	6.2	1	-0.0419	-0.0726	0.1243	0.0419	0.0726	0.1243	320.	0.50		
V(1, 0.6, 34, 270)	77	6.2	1	0	-0.0839	0.1243	0	0.0839	0.1243	310.	0.5	0.932	0.827
V(1, 0.6, 34, 300)	77	6.2	1	0.0419	-0.0726	0.1243	-0.0419	0.0726	0.1243	310.	0.50	0.933	0.828
V(1, 0.6, 34, 330)	77	6.2	1	0.0726	-0.0419	0.1243	-0.0726	0.0419	0.1243	310.	0.50	0.933	0.829
V(1, 0.6, 66, 0)	77	6.2	1	0.137	0	0.061	-0.137	0	0.061	270.	0.24		
V(1, 0.6, 66, 30)	77	6.2	1	0.1186	0.0685	0.061	-0.1186	-0.0685	0.061	270.	0.24		
V(1, 0.6, 66, 60)	77	6.2	1	0.0685	0.1186	0.061	-0.0685	-0.1186	0.061	270.	0.24		
V(1, 0.6, 66, 90)	77	6.2	1	0	0.137	0.061	0	-0.137	0.061	270.	0.24		
V(1, 0.6, 66, 120)	77	6.2	1	-0.0685	0.1186	0.061	0.0685	-0.1186	0.061	270.	0.24		
V(1, 0.6, 66, 150)	77	6.2	1	-0.1186	0.0685	0.061	0.1186	-0.0685	0.061	270.	0.24		
V(1, 0.6, 90, 0)	77	6.2	1	0.1499	0	0	-0.1499	0	0	220.	0	0.951	0.686
V(1, 0.6, 90, 30)	77	6.2	1	0.1299	0.075	0	-0.1299	-0.075	0	220.	0	0.951	0.684
V(1, 0.6, 90, 45)	77	6.2	1	0.106	0.106	0	-0.106	-0.106	0	210.	0.	0.95	0.683
V(1, 0.6, 90, 60)	77	6.2	1	0.075	0.1299	0	-0.075	-0.1299	0	200.	0.	0.95	0.681
V(1, 0.6, 90, 90)	77	6.2	1	0	0.1499	0	0	-0.1499	0	200.	0	0.949	0.68
V(1, 0.6, 90, 120)	77	6.2	1	-0.075	0.1299	0	0.075	-0.1299	0	210.	0	0.95	0.682
V(1, 0.6, 90, 150)	77	6.2	1	-0.1299	0.075	0	0.1299	-0.075	0	210.	0	0.951	0.685
V(1, 0.6, 90, 180)	77	6.2	1	-0.1499	0	0	0.1499	0	0	220.	0	0.951	0.686
V(1, 0.6, 90, 210)	77	6.2	1	-0.1299	-0.075	0	0.1299	0.075	0	220.	0	0.951	0.684
V(1, 0.6, 90, 240)	77	6.2	1	-0.075	-0.1299	0	0.075	0.1299	0	220.	0.	0.95	0.681
V(1, 0.6, 90, 270)	77	6.2	1	0	-0.1499	0	0	0.1499	0	220.	0	0.949	0.68
V(1, 0.6, 90, 300)	77	6.2	1	0.075	-0.1299	0	-0.075	0.1299	0	220.	0	0.95	0.682
V(1, 0.6, 90, 330)	77	6.2	1	0.1299	-0.075	0	-0.1299	0.075	0	220.	0	0.951	0.685
z(1,0)	103	10	1.	0	0	0	0	0	0	960.	0.	0.952	0.686
z(1,0)	100	10	1	0	0	0	0	0	0	930.	0.	0.951	0.687
z(1,0, 11,a)	120	11	1	0	0	0	0	0	0	1300.	0.	0.951	0.686
z(1, 0, 11,b)	160	11	1	0	0	0	0	0	0	1400.	0.	0.952	0.686
z(1, 0, 11,c)	200	11	1	0	0	0	0	0	0	1400.	0.	0.952	0.686
z(1, 0, 11,d)	240	11	1	0	0	0	0	0	0	1400.	0.	0.952	0.686
zq(1.15,0)	103	10	1.15	0	0	0	0	0	0	960.	0.	0.952	0.684
zq(1.25,0)	100	10	1.25	0	0	0	0	0	0	960.	0.	0.952	0.68
zq(1.3,0)	103	10	1.3	0	0	0	0	0	0	970.	0.	0.953	0.677
zq(1.45,0)	103	10	1.45	0	0	0	0	0	0	980.	0.	0.955	0.667
zq(1.5,0)	103	10	1.5	0	0	0	0	0	0	990.	0.	0.955	0.664
zq(1.5,0)	100	10	1.5	0	0	0	0	0	0	1000.	0.	0.955	0.664
zq(1.5,0, 11)	200	11	1.5	0	0	0	0	0	0	1400.	0.	0.955	0.664

zq(1.6,0)	103	10	1.6	0	0	0	0	0	0	990.	0.	0.956	0.656
zq(1.75,0)	103	10	1.75	0	0	0	0	0	0	1000.	0.	0.958	0.644
zq(1.9,0)	103	10	1.9	0	0	0	0	0	0	1000.	0.	0.96	0.632
zq(2,0)	103	10	2.	0	0	0	0	0	0	1000.	0.	0.961	0.623
zq(2,0)	100	10	2.	0	0	0	0	0	0	1000.	0.	0.961	0.623
zq(2.05,0)	103	10	2.05	0	0	0	0	0	0	1000.	0.	0.962	0.619
zq(2.2,0)	103	10	2.2	0	0	0	0	0	0	1100.	0.	0.963	0.606
zq(2.35,0)	103	10	2.35	0	0	0	0	0	0	1100.	0.	0.965	0.593
zq(2.5,0)	103	10	2.5	0	0	0	0	0	0	1100.	0.	0.967	0.581
zq(2.5,0, 11)	200	11	2.5	0	0	0	0	0	0	1600.	0.	0.967	0.581
zq(3,0)	200	11	3	0	0	0	0	0	0	1700.	0.	0.971	0.54
zq(4, 0,11)	200	11	4	0	0	0	0	0	0	2000.	0.	0.978	0.472
z(1,-0.4, 11)	200	11	1	0	0	-0.1	0	0	-0.1	1100.	-0.40	0.96	0.56
z(1, -0.2, 11)	200	11	1	0	0	-0.05	0	0	-0.05	1200.	-0.20	0.956	0.624
z(1, 0.2)	100	10	1	0	0	0.05	0	0	0.05	1100.	0.20	0.945	0.746
z(1, 0.2, 11)	200	11	1	0	0	0.05	0	0	0.05	1500.	0.20	0.945	0.746
zq(1.25 , 0.2)	100	10	1.25	0	0	0.0617	0	0	0.0395	1100.	0.2	0.946	0.74
zq(1.5, 0.2)	100	10	1.5	0	0	0.072	0	0	0.032	1100.	0.2	0.949	0.729
zq(1.5, 0.2, 11)	200	11	1.5	0	0	0.072	0	0	0.032	1600.	0.2	0.949	0.729
zq(1.75, 0.2)	100	10	1.75	0	0	0.081	0	0	0.0264	1200.	0.2	0.952	0.714
zq(2, 0.2)	100	10	2.	0	0	0.0889	0	0	0.0222	1200.	0.2	0.956	0.698
zq(2, 0.2, 11)	160	11	2.	0	0	0.0889	0	0	0.	1700.	0.2	0.956	0.698
z(1, 0.4, 11)	200	11	1	0	0	0.1	0	0	0.1	1700.	0.40	0.938	0.804
zq(1.25, 0.4)	100	10	1.25	0	0	0.1234	0	0	0.079	1200.	0.4	0.939	0.8
zq(1.5, 0.4)	100	10	1.5	0	0	0.144	0	0	0.064	1300.	0.4	0.941	0.792
zq(1.5, 0.4)	200	11	1.5	0	0	0.144	0	0	0.064	1700.	0.4	0.942	0.792
zq(1.75, 0.4)	100	10	1.75	0	0	0.162	0	0	0.0529	1300.	0.4	0.945	0.781
zq(2,, 0.4)	100	10	2.	0	0	0.1778	0	0	0.0444	1300.	0.4	0.949	0.768
zq(2, 0.4, 11)	160	11	2.	0	0	0.1778	0	0	0.0444	1900.	0.4	0.949	0.77
z(1, 0.6)	100	10	1	0	0	0.15	0	0	0.15	1400.	0.60	0.926	0.858
z(1, 0.6,11)	200	11	1	0	0	0.15	0	0	0.15	1900.	0.60	0.927	0.858
zq(1.25, 0.6)	100	10	1.25	0	0	0.1852	0	0	0.1185	1400.	0.6	0.928	0.855
zq(1.5, 0.6)	100	10	1.5	0	0	0.216	0	0	0.096	1400.	0.6	0.931	0.851
zq(1.75, 0.6)	100	10	1.75	0	0	0.243	0	0	0.0793	1400.	0.6	0.935	0.845
zq(2, 0.6)	100	10	2.	0	0	0.2666	0	0	0.0666	1500.	0.6	0.939	0.839
zq(2, 0.6,11)	160	11	2.	0	0	0.2666	0	0	0.0666	2000.	0.6	0.94	0.839
z(1, 0.8)	100	10	1	0	0	0.2	0	0	0.2	1500.	0.80	0.912	0.908
z(1, 0.8, 11)	200	11	1	0	0	0.2	0	0	0.2	1900.	0.8	0.912	0.909
zU(1, 0., 0.2, 11)	160	11	1	0	0	0	0	0	0.05	1400.	0.10	0.949	0.716
zU(1, 0., 0.4, 11)	160	11	1	0	0	0	0	0	0.1	1500.	0.20	0.945	0.746
zU(1, 0., 0.6, 11)	160	11	1	0	0	0	0	0	0.15	1600.	0.30	0.942	0.775
zU(1, 0., 0.8, 11)	160	11	1	0	0	0	0	0	0.2	1700.	0.40	0.937	0.802
zU(1, 0.2, 0.4, 11)	160	11	1	0	0	0.05	0	0	0.1	1600.	0.30	0.942	0.775
zU(1, 0.2, 0.6, 11)	160	11	1	0	0	0.05	0	0	0.15	1700.	0.40	0.937	0.803
zU(1, 0.2, 0.8, 11)	160	11	1	0	0	0.05	0	0	0.2	1700.	0.50	0.932	0.83